

AD _____

Award Number: DAMD17-01-1-0713

TITLE: Proton MR Spectroscopic Imaging in NF-1

PRINCIPAL INVESTIGATOR: Peter B. Barker, Ph.D.

CONTRACTING ORGANIZATION: Johns Hopkins University
Baltimore, Maryland 21205

REPORT DATE: July 2002

TYPE OF REPORT: Annual

PREPARED FOR: U.S. Army Medical Research and Materiel Command
Fort Detrick, Maryland 21702-5012

DISTRIBUTION STATEMENT: Approved for Public Release;
Distribution Unlimited

The views, opinions and/or findings contained in this report are those of the author(s) and should not be construed as an official Department of the Army position, policy or decision unless so designated by other documentation.

20030313 157

REPORT DOCUMENTATION PAGEForm Approved
OMB No. 074-0188

Public reporting burden for this collection of information is estimated to average 1 hour per response, including the time for reviewing instructions, searching existing data sources, gathering and maintaining the data needed, and completing and reviewing this collection of information. Send comments regarding this burden estimate or any other aspect of this collection of information, including suggestions for reducing this burden to Washington Headquarters Services, Directorate for Information Operations and Reports, 1215 Jefferson Davis Highway, Suite 1204, Arlington, VA 22202-4302, and to the Office of Management and Budget, Paperwork Reduction Project (0704-0188), Washington, DC 20503

1. AGENCY USE ONLY (Leave blank)		2. REPORT DATE July 2002	3. REPORT TYPE AND DATES COVERED Annual (1 Jul 01 - 30 Jun 02)	
4. TITLE AND SUBTITLE Proton MR Spectroscopic Imaging in NF-1			5. FUNDING NUMBERS DAMD17-01-1-0713	
6. AUTHOR(S) Peter B. Barker, Ph.D.				
7. PERFORMING ORGANIZATION NAME(S) AND ADDRESS(ES) Johns Hopkins University Baltimore, Maryland 21205 E-Mail: barker@mri.jhu.edu			8. PERFORMING ORGANIZATION REPORT NUMBER	
9. SPONSORING / MONITORING AGENCY NAME(S) AND ADDRESS(ES) U.S. Army Medical Research and Materiel Command Fort Detrick, Maryland 21702-5012			10. SPONSORING / MONITORING AGENCY REPORT NUMBER	
11. SUPPLEMENTARY NOTES				
12a. DISTRIBUTION / AVAILABILITY STATEMENT Approved for Public Release; Distribution Unlimited				12b. DISTRIBUTION CODE
13. Abstract (Maximum 200 Words) (abstract should contain no proprietary or confidential information) Neurofibromatosis Type 1 (NF-1) is the most common autosomal dominant genetic disorder, affecting the skin, central (CNS) and peripheral nervous systems. Children with NF-1 have an increased risk of developing significant learning disability (LD), cognitive impairment, and optic or brain stem gliomas. Cerebral magnetic resonance imaging (MRI) in NF-1 reveals regions of high signal intensity (often called "unidentified bright objects", or UBOs). The pathophysiology of UBOs is poorly understood, and it is controversial to what extent they are involved in cognitive impairment. The aims of this proposal are to characterize the underlying metabolic abnormalities in NF-1 with proton MR spectroscopic imaging (MRSI). We have developed a rapid, quantitative MR spectroscopic imaging (MRSI) protocol for the evaluation of cerebral metabolite levels in NF-1. Metabolite levels will be determined both in UBOs and other brain regions, both in order to improve understanding of the etiology of UBOs, and to understand the relationship between regional brain metabolism and LD. 60 subjects with NF1 and 60 control subjects will be evaluated with proton MRSI and detailed neuropsychological testing. Ultimately, proton MRSI may be a useful test for identifying children with NF-1 at risk of developing LD, and also help in distinguishing UBOs from other, malignant lesions which require therapeutic intervention.				
14. SUBJECT TERMS neurofibromatosis Type 1, magnetic resonance spectroscopy, magnetic resonance imaging, diagnosis			15. NUMBER OF PAGES 31	
			16. PRICE CODE	
17. SECURITY CLASSIFICATION OF REPORT Unclassified	18. SECURITY CLASSIFICATION OF THIS PAGE Unclassified	19. SECURITY CLASSIFICATION OF ABSTRACT Unclassified	20. LIMITATION OF ABSTRACT Unlimited	

Table of Contents

Cover	1
SF 298	2
Table of Contents	3
Introduction	4
Body	6
Key Research Accomplishments	11
Reportable Outcomes	12
Conclusions	13
References	14
Appendices	15

Introduction

Neurofibromatosis Type 1 (NF-1) is the most common autosomal dominant genetic disorder, affecting the skin, central (CNS) and peripheral nervous systems. Children with NF-1 have an increased risk of developing significant learning disability (LD), cognitive impairment, and optic or brain stem gliomas. Cerebral T₂-weighted magnetic resonance imaging (MRI) in NF-1 reveals regions of high signal intensity (often called "unidentified bright objects", or UBOs) in the basal ganglia, brain stem and cerebellum. The pathophysiology of UBOs is poorly understood, and it is controversial to what extent they are involved in cognitive impairment. Proton magnetic resonance spectroscopic imaging (MRSI) is a relatively new non-invasive metabolic imaging technique which can provide information about the cellular composition and metabolism of brain tissue. Our pilot data of proton MRSI in NF-1 indicate highly significant perturbations in thalamic metabolism in NF-1, regardless of presence or absence of UBOs. UBOs themselves were metabolically more similar to normal brain tissue. These data indicate a dissociation between imaging and metabolic findings, and may indicate more widespread cerebral involvement in NF-1 than that indicated by MRI.

In this proposal, we are extending these preliminary findings to investigate the hypotheses that: (1) thalamic metabolism is abnormal in NF-1 and evolves with age, (2) proton MRSI measures of thalamic metabolism will correlate with neuropsychological performance, and (3) metabolic abnormalities in NF-1 are more diffuse and widespread than abnormalities visualized by MRI. The study design to test these hypotheses involves the performance of proton MRSI, MRI and neuropsychological testing in 60 subjects with NF-1 and 60 age-matched control subjects. To test hypothesis (1), thalamic metabolite levels will be compared between NF-1 subjects and controls in 3 different age ranges, and regression analysis performed with respect to age. To test hypothesis (2) thalamic metabolite levels in NF-1 patients will be correlated with results of a battery of neuropsychological tests. To test hypothesis (3), multiple regions of interest in the basal ganglia and cerebellum will be evaluated both by MRI and MRSI, and compared between NF-1 and control subjects.

In addition to improving the understanding of the pathophysiology of NF-1 brain lesions, this proposal will establish the relationship between regional cerebral metabolism and cognitive impairment

in NF-1. If successful, MRSI may serve as a screening tool for young children with NF-1; the observation of normal MRSI may be reassuring prognostic information for normal subsequent development, while children with abnormal MRSI may be identified for early intervention for possible learning or developmental problems.

Body

Year 1 of this project has mainly been occupied with protocol development and optimization of study design, mainly as the result of prolonged difficulties with obtaining human subjects approval for the initiation of the clinical trial research component. A prerequisite for obtaining quantitative, localizer proton MRSI data in children is the establishment of a rapid (motion insensitive) multi-slice sequence with both good sensitivity and high spatial resolution. We have developed this sequence during year 1 and results were presented at the 2001 RSNA meeting and in the 2002 magnetic resonance in medicine journal article. In addition, quantitative measurements of metabolite concentrations requires an accurate measurement of cerebral spinal fluid (CSF) partial volumes. Traditionally, this is accomplished using high resolution but time consuming magnetic resonance imaging techniques; we have developed an alternative approach which utilizes single short fast spin echo MRI with scan time of only a few seconds, and also very simple post-processing methods. We have also designed and optimized the full suite of neuropsychological tests which will be used to probe learning disability and cognitive impairment in NF-1.

We are interested in evaluating the biochemical composition of UBOs as a function of age, as well as the examination of adjacent brain parenchyma in NF-1, as well as cerebral metabolism in patients without UBOs. We have examined a well-characterized group of subjects with a range of phenotypic expression of NF-1, and age- and sex-matched control subjects. Based on postmortem and imaging data described above, we hypothesized that the pathologic process underlying UBOs is relatively diffuse in nature, therefore, may be underestimated by conventional MRI. We circumscribed our measurements to supratentorial regions, considering that these locations consistently demonstrate UBOs with an age-dependent involution.

Nine male NF-1 patients (age range, 6-19 years; median, 12 years), 4 with normal MRI, and 5 with UBOs, which were participants in a research program aiming at characterizing the neurobehavioral phenotype of NF-1, constituted the experimental sample. All subjects were seizure-free and only one, in the subset with UBOs, had a small optic pathway glioma. So far, only the neuroimaging data and MRSI has been evaluated in these cases. The control group consisted of 9 sex-matched subjects (age range, 6-

19; median, 14 years) without any history of neurological disease and with normal brain MRI. All subjects were examined with conventional MRI and quantitative, multi-slice MRSI (for details, see methods section).

All subjects that, in the present sample, showed supratentorial UBOs had these abnormalities predominantly in the globus pallidus/internal capsule region. Accordingly, on one slice of the MRSI data set, regions of interest were identified in the thalamus, basal ganglia, and occipital gray matter. The latter region, which is typically uninvolved by hyperintense foci, served as an internal control. At least 2 pixels were identified which were completely encompassed by each structure, and each structure was measured in both left and right hemispheres. Since no left-right asymmetry could be identified, data from left and right hemispheres were averaged together before further statistical analysis. For each region of interest, absolute metabolite concentrations were calculated using the phantom replacement method (see methods section) which we have previously developed and validated. Metabolite ratios were also calculated for comparison with other, non-quantitative studies. Ratios are also insensitive to partial volume effects with CSF and potential systematic quantitation errors, and in some circumstances (e.g. when Cho increases and NAA decreases) ratios may be more sensitive (i.e. the NAA/Cho ratio) to detecting small changes than measurements of either metabolite concentration alone. For visual screening of MRSI data, metabolic images of individual metabolites were also recreated (Cho, 3.34-3.14 ppm; Cr, 3.14-2.94 ppm; NAA, 2.22-1.82 ppm; lactate, (not detected) 1.55-1.15 ppm).

Descriptive statistics consisted of calculation of means and standard deviations of metabolite concentrations and ratios. Due to the small sample size, metabolite concentrations and ratios were then compared between conditions using non parametric tests. We specifically used a variation of the Wilcoxon test, termed Robust Rank Order test (55). Both one- and two-tailed tests were applied. The latter does not assume a particular direction of the changes experienced by the experimental group, whereas the former applies to situations with predictable outcome. In this particular study, we hypothesized that the changes in metabolites will include decreases in NAA, due to white matter edema and/or neuronal injury, and increases in Cho as a consequence of high turnover of myelinic membranes

and/or gliosis. Therefore, one-tailed distributions of measurements were also considered. Data and statistical analyses were done using the Statview 5.0™ program.

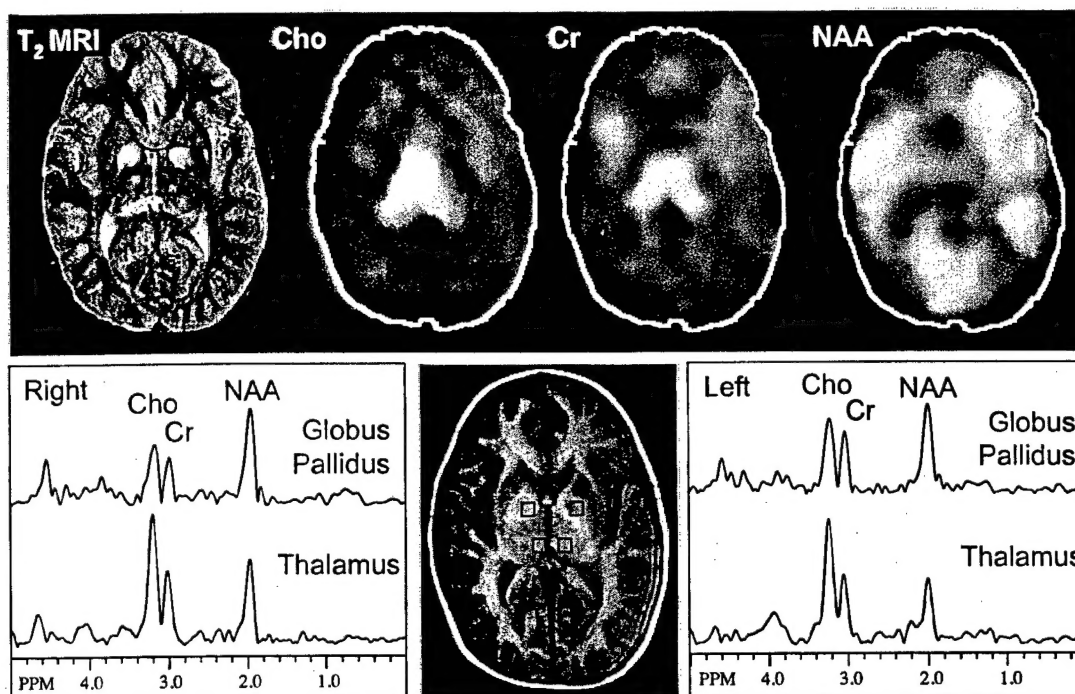


Figure 1. T1, T2 MRI and proton MRSI in an 8 year old NF-1 patient with prominent UBOs in globus pallidus/internal capsule and subtle thalamic UBOs. Metabolic images and spectra from both thalami show large increases in choline, while UBOs (in the globus pallidus) are relatively normal.

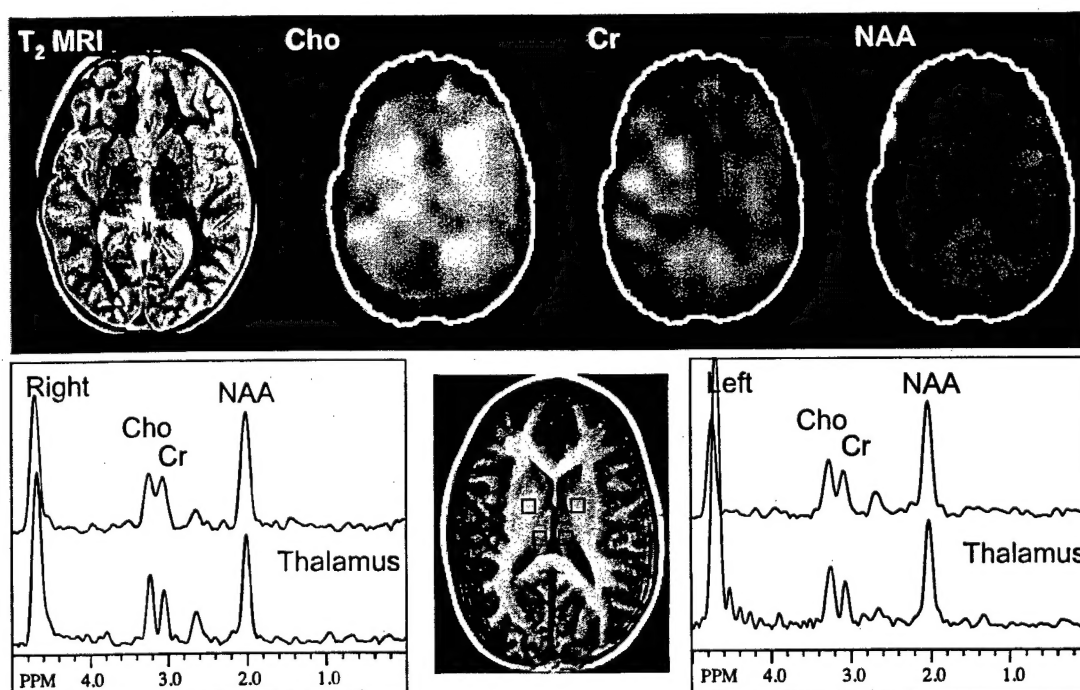


Figure 2. T1, T2 MRI and proton MRSI in an 8 year old control subject.

Figure 1 shows an example of MRI and proton MRSI in an 8 year old subject with prominent UBOs in the globus pallidus and subtle thalamic UBOs. MRSI reveals high levels of Cho primarily in the thalamus, with more normal appearing spectra from the pallidal UBOs. For comparison, spectra and images from an 8 year old control subject are shown in Figure 2. Since qualitative evaluation of the data sets indicated abnormal metabolism in the thalamus, in addition to evaluating UBOs, we also quantitatively analyzed spectra from the thalamus and occipital gray matter (considered to be an uninvolved "control" region") in all subjects. Results of the quantitative analysis (absolute metabolite concentrations and ratios) for all subjects are given in Table 1.

TABLE 1. Metabolite concentrations (mM) and ratios in thalamus, globus pallidus (including UBOs, if present), and medial occipital gray matter (GM) in NF-1 and control subjects. Values highlighted in bold are significantly different ($\alpha < 0.05$). *Indicates NF-1 patients without UBOs in globus pallidus. **Indicates thalamic measurements in NF-1 patients with UBO in globus pallidus. Note that only 4 out of 9 control subjects had interpretable spectra from the globus pallidus.

			[Cho]	[Cr]	[NAA]	NAA/Cho	NAA/Cr	Cho/Cr
Thalamus	NF-1 (N=9)	Mean	2.56	6.47	5.64	1.04	1.74	1.74
		St Dev	0.71	1.31	0.99	0.20	0.29	0.39
	Controls (N=9)	Mean	1.95	6.04	7.45	1.71	2.52	1.50
		St Dev	0.45	1.70	1.75	0.19	0.17	0.19
	NF-1* (N=4)	Mean	2.28	6.05	5.94	1.19	1.95	1.69
		St Dev	0.31	0.95	0.93	0.12	0.09	0.17
	UBO** (N=5)	Mean	2.78	6.81	5.40	0.92	1.57	1.78
		St Dev	0.89	1.56	1.09	0.16	0.29	0.53
Globus Pallidus	NF-1* (N=4)	Mean	1.61	5.13	6.53	1.86	2.56	1.48
		St Dev	0.31	0.87	0.50	0.22	0.65	0.48
	UBO (N=5)	Mean	1.85	5.85	5.84	1.49	2.00	1.41
		St Dev	0.58	1.77	1.18	0.41	0.39	0.41
	Controls	Mean	1.72	5.00	6.20	1.71	2.58	1.60

	(N=4)	St Dev	0.46	0.82	0.34	0.41	0.53	0.38
Occipital GM	NF-1	Mean	1.38	5.33	7.09	2.24	2.58	1.16
	(N=9)	St Dev	0.41	1.15	1.93	0.36	0.57	0.24
	Controls	Mean	1.68	6.68	8.18	2.26	2.47	1.13
	(N=9)	St Dev	0.39	1.04	1.53	0.33	0.31	0.28

Key Research Accomplishments

- Establishment of a rapid multi-slice proton MRSI examination suitable for studies in children
- Design and validation of an MRSI quantitation scheme which corrects for partial volume of CSF with minimal scan time and simple post-processing requirements
- The demonstration of abnormal, age-dependent thalamic metabolism in children with NF-1

Reportable Outcomes

The following journal articles have been published (or are in press) this year:

- Golay X, Gillen J, van Zijl PCM, Barker PB. *Scan Time Reduction in Proton Magnetic Resonance Spectroscopic Imaging of the Human Brain*. Magnetic Resonance in Medicine 2002; **47**:384-7
- Horská A, Calhoun V, Bradshaw D, Barker PB. *A rapid method for correction of CSF partial volume in quantitative proton MR spectroscopic imaging*. Magn. Reson. Med. 2002; (in press)

Conclusions

In year 1 of this protocol we have established a quantitative, multi-slice proton MRSI protocol with short scan duration which is well suited for the evaluation of children with NF-1. With this methodology now in place, the collection of data for the evaluation of the relationship between neurometabolism, in particular thalamic NAA and choline levels (and the ratio of NAA/Cho), and LD in NF-1 will take place in years 2 and 3.

This work is important for the clinical evaluation of patients with NF-1 in two respects. Firstly, proton MRSI may allow for a quantitative biochemical determination of the degree of brain involvement in children with NF-1, the observation of normal MRSI may be reassuring prognostic information for normal subsequent development, while children with abnormal MRSI may be identified for early intervention for possible learning or developmental problems. Secondly, the characterization of UBO metabolism is important for the diagnostic reasons; since patients with NF-1 are at increased risk for development of brain and optic gliomas, it can sometimes be difficult to distinguish these very different pathologies using conventional magnetic resonance imaging. Early, non-invasive diagnosis of a malignant glioma (and distinguishing it from a benign UBO) is extremely important in improving therapeutic outcome in these patients.

References

- Wang PY, Kaufman WE, Koth CW, Denckla MB, Barker PB. *Thalamic Involvement In Neurofibromatosis Type 1: Evaluation With Proton MR Spectroscopic Imaging*. Ann Neurol 2000; **47**:477-484
- Barker PB, Golay X, Gillen J, van Zijl PCM. *Scan Time Reduction in Proton MR Spectroscopic Imaging of the Human Brain*. RSNA Chicago, IL, 2001;
- Golay X, Gillen J, van Zijl PCM, Barker PB. *Scan Time Reduction in Proton Magnetic Resonance Spectroscopic Imaging of the Human Brain*. Magnetic Resonance in Medicine 2002; **47**:384-7
- Horská A, Calhoun V, Bradshaw D, Barker PB. *A rapid method for correction of CSF partial volume in quantitative proton MR spectroscopic imaging*. Magn. Reson. Med. 2002; (in press)

Appendices

- Wang PY, Kaufman WE, Koth CW, Denckla MB, Barker PB. *Thalamic Involvement In Neurofibromatosis Type 1: Evaluation With Proton MR Spectroscopic Imaging.* Ann Neurol 2000; **47**:477-484
- Golay X, Gillen J, van Zijl PCM, Barker PB. *Scan Time Reduction in Proton Magnetic Resonance Spectroscopic Imaging of the Human Brain.* Magnetic Resonance in Medicine 2002; **47**:384-7
- Horská A, Calhoun V, Bradshaw D, Barker PB. *A rapid method for correction of CSF partial volume in quantitative proton MR spectroscopic imaging.* Magn. Reson. Med. 2002; (in press)

Thalamic Involvement in Neurofibromatosis Type 1: Evaluation with Proton Magnetic Resonance Spectroscopic Imaging

Paul Y. Wang, MD,* Walter E. Kaufmann, MD,†‡§¶ Christine W. Koth, MS,¶ Martha B. Denckla, MD,‡§¶ and Peter B. Barker, DPhil*¶

Neurofibromatosis type 1 is a common autosomal dominant disorder associated with learning disabilities. In addition to gliomas and other tumors, T2 hyperintense lesions (unidentified bright objects or UBOs) are frequently found in the globus pallidus, cerebellum, and white matter regions. To better characterize supratentorial UBO functional significance, we studied by quantitative magnetic resonance spectroscopic imaging (MRSI) 9 male subjects with neurofibromatosis type 1 (age, 6–19 years) and 9 age-matched and sex-matched controls. Maps of the anatomical distribution of the metabolites choline (Cho), *N*-acetylaspartate (NAA), and creatine were calculated in four axial 15-mm slices. Absolute metabolite concentrations within UBOs, unaffected globus pallidus, and thalami demonstrated an age-related pattern, characterized by elevated Cho and relatively preserved NAA in younger subjects (<10 years) and reduced NAA and normal Cho in older subjects. These changes were found in both UBOs and thalami but were only significant for NAA, NAA/creatine, and NAA/Cho in the latter region. Decreases in NAA ratios were most severe in the thalami of subjects with UBOs in the globus pallidus, whereas UBOs showed similar but milder abnormalities than those in the thalamus. We speculate that the MRSI metabolic abnormality may represent a more generalized phenomenon, without a T2 signal counterpart in the affected brain regions. Based on the neuropathological study by DiPaolo and colleagues (1995), we postulate that Cho elevations reflect increased myelin turnover in areas of intramyelinic edema, which is followed by neuropil injury (reduced NAA). Temporal progression and behavioral correlates of these MRSI changes deserve further exploration.

Wang PY, Kaufmann WE, Koth CW, Denckla MB, Barker PB. Thalamic involvement in neurofibromatosis type 1: evaluation with proton magnetic resonance spectroscopic imaging. *Ann Neurol* 2000;47:477–484

Neurofibromatosis type 1 (NF-1) is the most common autosomal dominant genetic disorder that affects the skin and the central (CNS) and peripheral nervous systems.¹ The most frequent NF-1 manifestations in the brain are primary CNS tumors and cognitive impairment. The incorporation of magnetic resonance imaging (MRI) with the NF-1 diagnostic battery demonstrated another type of CNS abnormality, ie, unidentified bright objects or UBOs.^{2,3} These are high signal-intensity foci on T2-weighted images, which are preferentially located in basal ganglia, cerebellum, and white matter regions.^{2–5} The pathogenesis of UBOs and their role in NF-1-associated learning disability remain still unclear. Nevertheless, some unique features of these high signal-intensity abnormalities have been described. UBO size seems to decrease over time, particularly in their most characteristic supratentorial localization, the globus pallidus (GP).^{3–8} There is evi-

dence that the presence of UBOs represents a risk factor for NF-1 learning disability. An early study showed that IQ and language scores were lower, and impairment in visuomotor function more frequent, in children with UBOs compared with a group without these hyperintense lesions.⁷ More recently, Denckla and colleagues⁹ suggested that number of UBO locations rather than relative volume of CNS parenchymal involvement explained IQ lowering in children with NF-1.

One neuropathological analysis of 3 cases demonstrated spongiotic changes in correspondence with T2 hyperintensities in GP, internal capsule (IC), and cortical white matter.¹⁰ These anomalies were characterized predominantly as vacuolar myelinic change, without associated demyelination, inflammation, or gliosis.¹⁰ This pathological study also indicated that the white matter changes were relatively widespread and extended into

From the Departments of *Radiology, †Pathology, ‡Neurology, §Pediatrics, and ¶Psychiatry and Behavioral Sciences, Johns Hopkins University School of Medicine, and ¶Kennedy Krieger Institute, Baltimore, MD.

Received Sep 14, 1999, and in revised form Nov 10. Accepted for publication Dec 1, 1999.

Address correspondence to Dr Barker, Department of Radiology, MRI 143C, Johns Hopkins University School of Medicine, 600 N. Wolfe Street, Baltimore, MD 21287.

adjacent gray matter structures.¹⁰ These anatomical observations are in agreement with some of the imaging studies mentioned above, which emphasize the preferential distribution of UBOs in fiber bundles and cerebellar white matter.^{5,6}

Recently, the metabolism of UBOs has been investigated by using localized proton magnetic resonance spectroscopy (MRS).¹¹⁻¹³ Noninvasive metabolic measurements by proton MRS have helped to improve understanding of the underlying cellular composition of brain tissue.¹⁴ By using a single-voxel technique, it was shown that UBOs do not differ from normal brain but have higher *N*-acetylaspartate (NAA)/creatine (Cr) and Cr/choline (Cr/Cho) ratios than a group of non-NF-1 patients with gliomas.¹¹ In another study, from using a nonquantitative multivoxel spectroscopy technique,¹³ NF-1 patients with brainstem gliomas were shown to have elevated concentrations of Cho and reduced or absent NAA, whereas UBO and peri-UBO regions had elevated Cho but near normal NAA concentrations. Each of these studies had significant limitations; ie, neither used a quantitation methodology to calculate absolute metabolite concentrations, and the single-voxel technique used large voxel sizes (from 8 to 27 cm³) and could cover very limited regions of the brain.¹¹ The multivoxel study was restricted to only 5 NF-1 children, all of whom had both gliomas and UBOs, and 2 non-age-matched controls. In the present study, therefore, we attempted to reevaluate the biochemical composition of brain in NF-1, both in patients with UBOs and adjacent parenchyma, and in patients without UBOs, by quantitative, high-resolution, multislice MRS imaging (MRSI). We examined a well-characterized group of subjects with a range of phenotypic expression of NF-1, and age-matched and sex-matched control subjects.

Patients and Methods

Study Design

Nine male NF-1 patients (ages 6, 8, 8, 9, 12, 14, 15, 16, and 19 years; median, 12 years), 4 with normal MRI scans, and 5 with UBOs, who were participants in a research program that tried to characterize the neurobehavioral phenotype of NF-1, constituted the experimental sample. All subjects were seizure-free and only 1, in the subset with UBOs, had a small optic pathway glioma. For the purposes of the present investigation, only neuroimaging data were analyzed. The control group consisted of 9 sex-matched subjects (ages 6, 10, 12, 13, 14, 16, 16, 18, and 19 years; median, 14 years) without any history of neurological disease and with normal brain MRI scans.

MRI Acquisition

All children were evaluated with routine brain MRI scans (T1-weighted and T2-weighted sequences) and multislice MRSI scans. All scans were performed on a 1.5-T General Electric (GE, Milwaukee, WI) Signa scanner by using the

standard GE quadrature head coil. The MR protocol consisted of the following series sagittal T1 and axial spin-density/T2-weighted brain MRI, followed by multislice MRSI. The technical details of the MRSI were as follows: repetition time, 2,300 msec; echo time, 280 msec; 15-mm slice; 2.5-mm gap; 24 × 24-cm field of view; 32 × 32 × 256 matrix; number of excitations, 1; 22-minute scan time, using a circularly encoded spin-echo sequence with water and octagonal outer volume lipid suppression.¹⁵ The sequence has been described in detail previously.¹⁵ In the current study, four slices were recorded, the most inferior of which was centered on the thalamus and GP (most frequent location of supratentorial UBOs), oriented parallel to the anterior/posterior commissure axis.

MRSI Data Analysis

Peak areas, frequencies, and linewidths were determined by fitting the three main resonances of the spectrum (Cho, 3.25 ppm; Cr, 3.06 ppm; and NAA, 2.02 ppm) to a Gaussian lineshape by using a "simplex" algorithm as described previously.¹⁶ For each brain region, both absolute metabolite concentrations and metabolite ratios were calculated. Metabolite concentrations were calculated by using the phantom replacement techniques as described previously (based on the power for a 90° pulse) and receiver gain, and truncation effects. Full details are provided in the article by Soher and associates.¹⁶ Metabolic images were calculated by using integration over a fixed frequency range for each resonance (Cho, 3.34–3.14; Cr, 3.14–2.94; NAA, 2.22–1.82; lactate, [not detected] 1.55–1.15) after applying a susceptibility correction based on the field maps generated from series.⁵ Metabolic images were linearly interpolated from the initial 32 × 32 matrix size to 256 × 256.

All subjects who, in the present sample, showed supratentorial UBOs had these abnormalities predominantly in the GP/IC region. Accordingly, on slice 1 of the MRSI data set, regions of interest were identified in the thalamus, basal ganglia, and occipital gray matter. The latter region, which is typically uninvolved by hyperintense foci,⁵ served as an internal control. At least two pixels were identified that were completely encompassed by each structure, and each structure was measured in both left and right hemispheres. Because no left/right asymmetry could be identified, data from left and right hemispheres were averaged together before further statistical analysis. GP data were available on only 4 of 9 control subjects, either because the slice positioning did not allow good visualization of the structure or because of field inhomogeneity problems. Difficulties in obtaining high-resolution spectra from the GP have been discussed previously (Barker PB, Horska A, Szopinski K, unpublished data).

Statistical Analyses

Descriptive statistics consisted of calculation of means and standard deviations of metabolite concentrations and ratios. Because of the small sample size, metabolite concentrations and ratios were then compared between conditions by using nonparametric tests. We specifically used a variation of the Wilcoxon test, termed the robust rank order test.¹⁷ Both one-tailed and two-tailed tests were applied. The latter does not assume a particular direction of the changes experienced

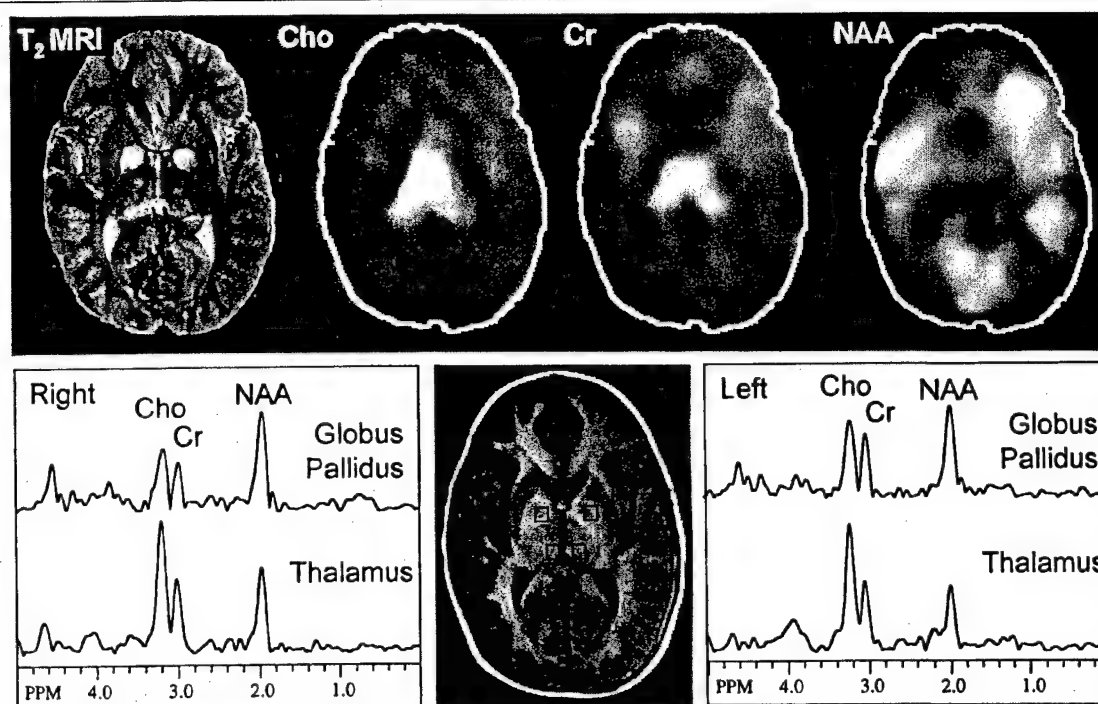


Fig 1. Proton magnetic resonance spectroscopic imaging and magnetic resonance imaging (MRI) images in an 8-year-old neurofibromatosis type 1 patient with prominent unidentified bright objects (UBOs) in globus pallidus and subtle thalamic UBOs. Spectra from the thalamus show a large increase in choline, whereas UBOs (in the globus pallidus) are relatively normal. Cho = choline; Cr = creatine; NAA = N-acetylaspartate.

by the experimental group, whereas the former applies to situations with predictable outcome. In this particular study, we hypothesized that the changes in metabolites will include decreases in NAA, because of white matter edema and/or neuronal injury, and increases in Cho as a consequence of high turnover of myelinic membranes and/or gliosis. Therefore, one-tailed distributions of measurements were also considered. Data and statistical analyses were done by using the Statview 5.0' program.

Results

Qualitative Analyses

Routine spin-density/T2 MRI scans showed UBOs in the GP/IC region in 5 of 9 children with NF-1 (ages, 6, 8, 9, 14, and 19 years). The distribution of the UBOs was the following: left and right GP/IC (6 years old); left and right cerebral peduncle, left and right GP/IC with some bilateral extension to adjacent thalamus, small in both left and right posterior thalami (8 years old); multiple in left and right cerebellar white matter and right middle cerebellar peduncle, left and right GP/IC with some bilateral extension into adjacent thalamus (9 years old); right cerebral peduncle, left and right GP/IC with some thalamic extension on the right (14 years old); and left GP/IC with extension

into thalamus (19 years old). The last subject also showed a small optic pathway glioma in the thalamic/optic radiation region without any relationship with the already mentioned UBO. It was observed that the 14- and 19-year-old subjects with UBOs had smaller lesions than on previous MRI scans in the same subjects. The 15-year-old NF-1 subject had no visible UBOs at the time of the scan but had UBOs in previous scans. Several of the subjects also exhibited macrocephaly. No other lesions were identified in either the NF-1 or the control group.

Qualitative evaluation of metabolic images showed multiple areas of either reduced NAA or increased Cho concentrations in individual cases. Regions that showed these effects included, in addition to the thalamus and GP/IC, the cerebellar vermis, midbrain, and periventricular white matter. The most striking abnormality, particularly in the youngest NF-1 subjects, was a dramatic increase in Cho in the thalamus, even in the absence of obvious UBOs in this region as illustrated in Figure 1. In contrast, spectra from the UBOs in the GP/IC in this subject, shown in Figure 1, were relatively normal. Figure 2 shows spectra from a normal 8-year-old for comparison.

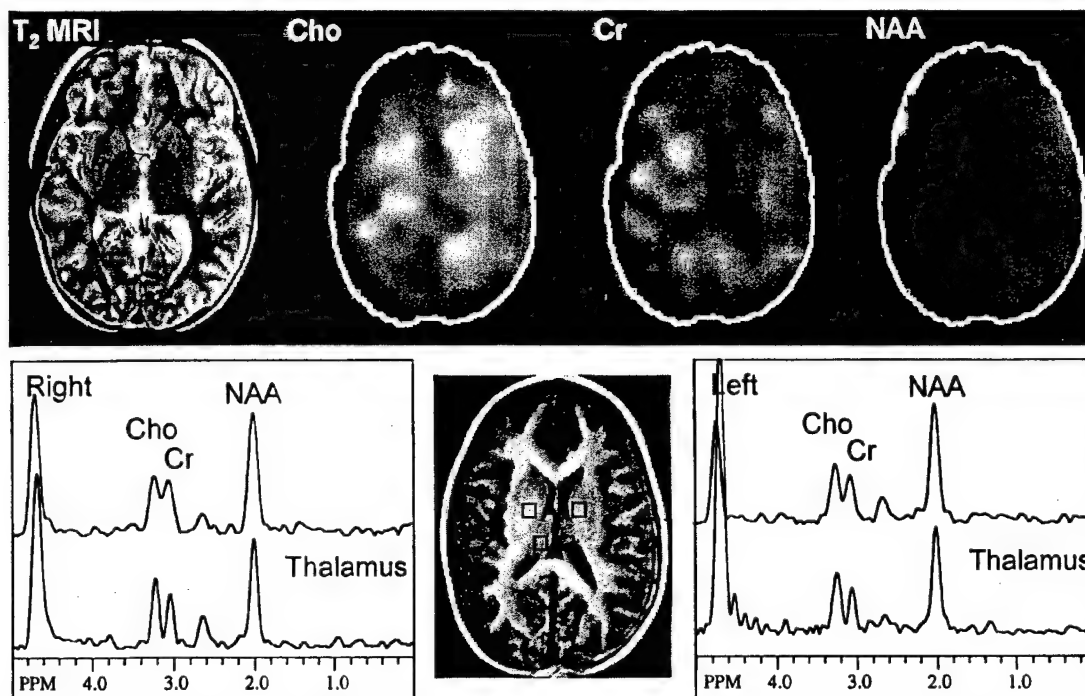


Fig 2. Proton magnetic resonance spectroscopic imaging and magnetic resonance imaging (MRI) images in an 8-year-old control subject. Cho = choline; Cr = creatine; NAA = N-acetylaspartate.

Quantitative Evaluations of Metabolites

Absolute metabolite concentrations and metabolite ratios for each region are given in the Table for each group. Figure 3 shows age-related changes in metabolite concentrations and ratios in the thalamus. Despite the dramatic increase in thalamic Cho in young subjects (see Figs 1 and 3), mean Cho concentration and Cho/Cr ratios were only 31% and 16% higher, respectively, in the NF-1 group than in the control subjects and were not significantly different by nonparametric testing. Inspection of Figure 3 shows that this is because the older NF-1 subjects (>9 years) have very similar thalamic Cho concentrations compared with control subjects. Thalamic NAA concentrations and NAA/Cr ratio were 24% and 31% lower in the affected children, and these were statistically significant by nonparametric testing (NAA: $p < 0.05$, two-tailed; $p < 0.025$, one-tailed; NAA/Cr: obviolate analysis, all subjects with NF-1 have ratios lower than any control). Figure 3 illustrates that this is mainly the result of lower NAA concentrations in the older NF-1 subjects compared with controls. The NAA/Cho ratio in the thalamus was 39% lower in subjects with NF-1, with no overlap between groups, and was highly significant (obviolate analysis, all subjects with NF-1 have NAA/Cho ratios lower than any control). In younger subjects, the decrease in this ratio appears to be mainly the

result of increased Cho, but in older subjects it is the result of decreased NAA (see Fig 3). Thalamic metabolite concentrations and ratios were also compared between NF-1 subjects with and without UBOs in the GP/IC. Although Cho concentrations were higher and NAA lower in subjects with GP/IC UBOs, these differences were not significant. However, ratios of thalamic NAA/Cho and NAA/Cr were significantly lower in NF-1 cases with (nonthalamic) UBOs by 29% and 24%, respectively ($p < 0.05$, two-tailed; $p < 0.025$, one-tailed, for both parameters).

In the GP, there was a trend for UBOs to have slightly higher Cho concentrations and lower NAA concentrations compared with either control subjects or NF-1 patients without UBOs, which led to 14% and 20% reductions in the NAA/Cho ratio, respectively. By contrast, pallidal tissue without UBOs did not show an increase in Cho or a decrease in NAA concentration compared with controls, but rather the opposite (−6% and +5%, respectively). However, no comparison of any metabolite concentration or ratio between groups in the pallidi reached statistical significance, in accordance with the qualitative observation of normal spectra in this region for all NF-1 subjects, with or without UBOs.

Statistical analysis of occipital gray matter showed a significant, 20% reduction in Cr in NF-1 compared

Table. Metabolite Concentrations (mM) and Ratios in Thalamus, Globus Pallidus (Including UBOs, If Present), and Medial Occipital Gray Matter in NF-1 and Control Subjects

	[Cho]	[Cr]	[NAA]	NAA/Cho	NAA/Cr	Cho/Cr
Thalamus						
NF-1 (n = 9)						
Mean	2.56	6.47	5.64	1.04	1.74	1.74
SD	0.71	1.31	0.99	0.20	0.29	0.39
Controls (n = 9)						
Mean	1.95	6.04	7.45	1.71	2.52	1.50
SD	0.45	1.70	1.75	0.19	0.17	0.19
NF-1 ^a (n = 4)						
Mean	2.28	6.05	5.94	1.19	1.95	1.69
SD	0.31	0.95	0.93	0.12	0.09	0.17
UBO ^b (n = 5)						
Mean	2.78	6.81	5.40	0.92	1.57	1.78
SD	0.89	1.56	1.09	0.16	0.29	0.53
Globus pallidus						
NF-1 ^a (n = 4)						
Mean	1.61	5.13	6.53	1.86	2.56	1.48
SD	0.31	0.87	0.50	0.22	0.65	0.48
UBO (n = 5)						
Mean	1.85	5.85	5.84	1.49	2.00	1.41
SD	0.58	1.77	1.18	0.41	0.39	0.41
Controls (n = 4) ^c						
Mean	1.72	5.00	6.20	1.71	2.58	1.60
SD	0.46	0.82	0.34	0.41	0.53	0.38
Occipital gray matter						
NF-1 (n = 9)						
Mean	1.38	5.33	7.09	2.24	2.58	1.16
SD	0.41	1.15	1.93	0.36	0.57	0.24
Controls (n = 9)						
Mean	1.68	6.68	8.18	2.26	2.47	1.13
SD	0.39	1.04	1.53	0.33	0.31	0.28

Values in boldface are significantly different ($\alpha < 0.05$).

^aNF-1 patients without UBOs in globus pallidus.

^bThalamic measurements in NF-1 patients with UBO in globus pallidus.

^cNote that only 4 of 9 control subjects had assessable spectra from the globus pallidus.

UBO = unidentified bright objects; NF-1 = neurofibromatosis type 1; Cho = choline; Cr = creatine; NAA = *N*-acetylaspartate.

with control subjects in both the one-tailed test (which hypothesized that Cr concentrations would be lower in this region) and the two-tailed test. Absolute concentrations of [Cho] were 18% lower and [NAA] 13% lower but did not reach statistical significance. All metabolite ratios in occipital gray matter were virtually identical between NF-1 and control subjects (4% difference or less). The most likely explanation for these findings (ie, essentially parallel reductions of all metabolite concentrations) is that the regions of interest used for analysis in occipital gray matter contained more cerebrospinal fluid (CSF) contamination in NF-1 subjects than controls. This may be the result of mild atrophy or sulcal enlargement. The quantitation procedure used in the current study does not correct for such partial volume effects; however, because CSF contains very low concentrations of metabolites, ratio measurements are unaffected by CSF contamination. Partial volume effects are larger for cortical regions than the other structures evaluated in this study (thalamus,

GP), which are large enough to be measured by ¹H MRSI with negligible CSF contamination.

Discussion

The major finding of this study is the presence of an abnormal pattern of metabolites, as measured by multislice MRSI, in the thalamus of children with NF-1. This abnormality (low NAA/Cho and NAA/Cr ratios) was found in all NF-1 cases under study, regardless of whether the patients did or did not have UBOs in the typical GP/IC location on MRI scan. It was found, however, that the biggest thalamic abnormalities were in patients with nonthalamic UBOs. In the 5 NF-1 cases who presented with UBOs in the GP/IC, the pattern of lower NAA and higher Cho concentrations was also found in these hyperintense foci, but the magnitude of the changes was considerably lower and did not reach statistical significance. This may be caused, in part, by partial volume effects with surrounding tissue in some of the patients with UBOs smaller than the

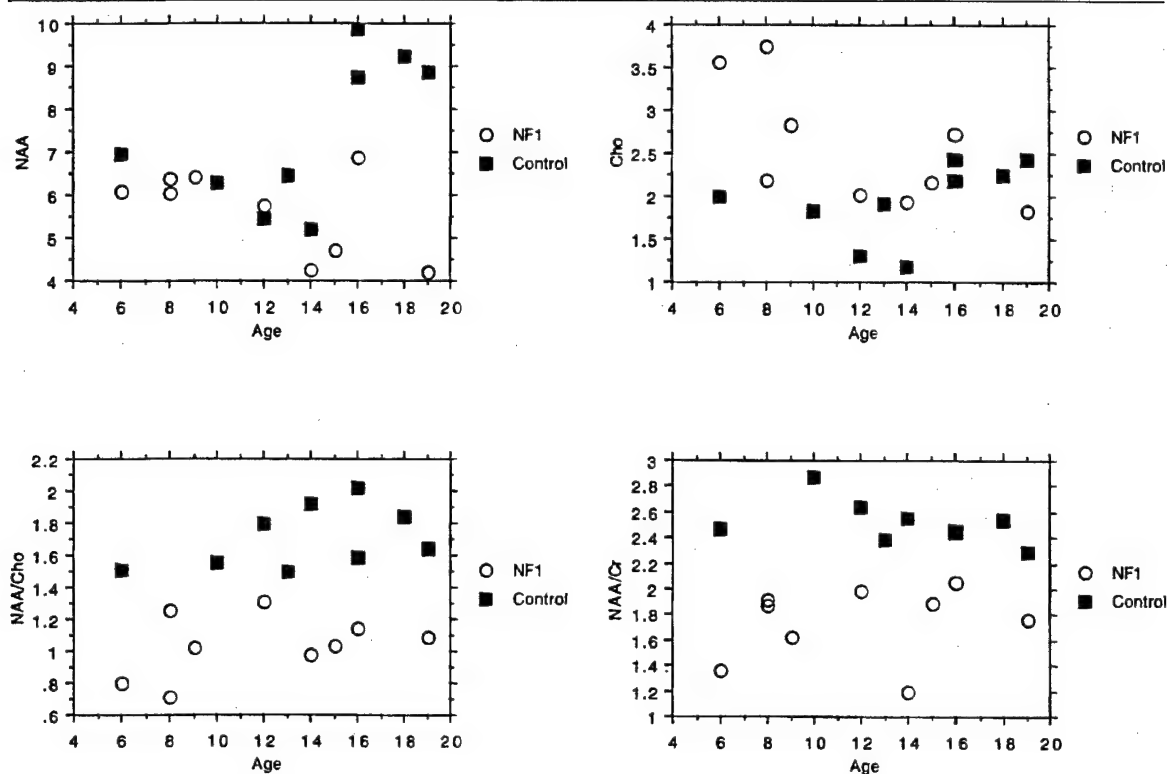


Fig 3. Absolute concentrations of N-acetylaspartate (NAA) and choline (Cho; mM), and ratios of NAA/Cho and NAA/creatine (NAA/Cr), in the thalamus in neurofibromatosis type 1 (NF-1) and control subjects. Young NF-1 subjects show high concentrations of Cho, whereas older NF-1 subjects have low concentrations of NAA; the ratios of NAA/Cho and NAA/Cr show complete separation between the groups.

MRSI voxel size (0.8 cm^3). The normal appearing pallidi in subjects with NF-1 were also indistinguishable from the same region in the control group.

There have been few previous reports of proton MRS or MRSI in NF-1, and no previous studies of thalamic metabolism in NF-1. Proton MRS studies in NF-1 have generally focused on the value of this technique in distinguishing benign UBOs from neoplastic lesions.¹¹⁻¹³ In particular, Castillo and colleagues¹¹ and Broniscer and co-workers¹² performed single-voxel measurements, which showed essentially normal metabolite ratios for UBOs compared with normal brain, but with markedly different ratios from either supratentorial¹¹ or diffuse pontine¹² gliomas, which had lower ratios of NAA/Cho. Consistent with these previous reports, we found mild but not significant differences in metabolite concentrations or ratios between the GP of NF-1 patients with or without UBOs, and normal subjects. However, other reports have suggested metabolic abnormalities in UBOs; although no statistical analysis was performed, Gonen and collaborators¹³ reported that UBOs "showed similar traits to optic pathway gliomas" (ie, high Cho) and "NAA levels

relatively unchanged compared with normal brain." They also reported that MRI normal appearing tissue near UBOs "exhibited similar behavior." It was also recently reported that a patient with a cerebellar UBO (which had spontaneously regressed) had high concentrations of Cho.¹⁸ Therefore, these reports indicate that UBO metabolism may depend on anatomical location and also stage of disease, because UBOs are also known to evolve with age.^{5,6}

In the current study, 2 of the 5 subjects with UBOs demonstrated foci that had decreased in size over time, and these GP/IC foci also showed the lowest Cho concentrations among UBOs. This observation is in agreement with the hypothesis that the disappearance of UBOs on MRI scan may reflect myelin repair,⁶ which would be consistent with a decrease in Cho, because the Cho resonance detected in *in vivo* proton MRS consists predominantly of the myelin membrane synthesis and degradation products, phosphocholine and glycerophosphocholine.¹⁹ Because the MRI appearance changes with time, it may be reasonable to expect that the metabolic abnormalities detected by MRSI could also be related to the stage of UBO evolution. In our

sample, there were some intriguing differences in the thalamic metabolite profile between younger and older subjects with NF-1 (see Fig 3). The former, which, as expected, had conspicuous UBOs, had the highest Cho concentrations. In contrast, older subjects showed relatively lower concentrations of NAA. Furthermore, the most marked thalamic changes were detected in individuals with UBOs. Our data seem to indicate that there is a relationship between GP/IC and thalamic metabolic abnormality and presence and involution of UBOs. Nevertheless, more definitive conclusions will require further studies because our patient group was relatively small and spanned a fairly wide age range (6–19 years).

One pathological/radiological correlation study of 3 cases reported spongiform myelinopathy or vacuolar change in myelin in regions with UBOs on MRI scan, and microcalcification of the GP in 1 case, but without any evidence of demyelination, axonal damage, or inflammation.¹⁰ The fluid-filled vacuoles were believed to be responsible for the increased signal seen on T2 MRI scan, although it was reported that vacuolation extended beyond the GP and IC (where UBOs were observed) and was also seen in cerebral peduncles, deep cerebellar white matter, optic tracts, and adjacent gray matter structures. Histopathology of the thalamus was not reported in these cases. It is noteworthy that the younger (neonatal) case demonstrated the most widespread changes that extended throughout cerebral and cerebellar white matter.¹⁰ This pathological report, in conjunction with previous imaging studies,^{5,6,20} supports that UBOs mainly represent intramyelinic edema and that the vacuolar changes are rather extensive but reversible to some extent. In the current study, the main abnormalities consisted in a mild increase in Cho and more severe decrease in NAA. Because gliosis does not appear to be a prominent process in NF-1, the most likely explanation is myelin membrane turnover. The relatively higher concentrations of Cho in younger subjects are in concordance with most extensive edema in younger NF-1 patients, as reported by DiPaolo and colleagues.¹⁰ The significance of the reduction in NAA concentrations, which seem to be more severe over time, is unclear. In addition to "neuropil dilution" secondary to edema, axonal injury is a plausible mechanism. The already mentioned pathological report¹⁰ does not describe axonal damage; however, the relatively less sensitive histological techniques and young age of the subjects may have contributed to these negative data.

The distribution of our MRSI abnormalities was unexpected. The resemblance in myelin packing between many thalamic nuclei and the GP,²¹ as well as the proximity between the medial thalamus and the pallidum, may explain the common involvement of these two structures. The mechanisms by which intramy-

elinic edema causes different imaging and spectroscopic manifestations in different anatomical locations remain to be determined, and it cannot be ruled out that there may be different underlying pathophysiological processes in the different structures. However, in support of the concept of diffuse cerebral abnormalities in NF-1, it has recently been demonstrated that small but significant T1 reductions are present in multiple structures such as corpus callosum, optic radiations, caudate, thalamus, and cerebral cortex in patients with NF-1.²² Another factor that might contribute to the conspicuous nature of UBOs in the GP is its unique cellular and mineral composition, which may have a greater impact on T2 signal than in other structures.

A higher frequency of learning disability, reflected among other variables as a general lowering of IQ, occurs in children affected with NF-1 relative to the general population.^{7,9,23} The presence of UBOs has been postulated as a potential mechanism that underlies learning disability in NF-1. In favor of this hypothesis, North and associates⁷ reported that children with UBOs had lower IQ scores than those without UBOs, whereas Denckla and associates⁹ found a continuum of lowered IQs correlating with the number of anatomical locations occupied by UBOs. In contrast with the latter study, Moore and co-workers²⁴ reported that only UBOs in the thalamus, not those in the typical GP/IC location, affected IQ and other measures of cognitive and motor scores. This study is intriguing because the current investigation showed predominantly abnormal thalamic metabolism in NF-1, and future studies are therefore required to correlate thalamic metabolite concentrations with quantitative measures of cognitive impairment.

We conclude that the MRSI metabolic abnormality in UBOs represents a more generalized phenomenon without a T2 signal counterpart in the affected brain regions. Based on the neuropathological study by DiPaolo and colleagues,¹⁰ we postulate that early thalamic Cho elevations reflect increased myelin turnover in areas of intramyelinic edema, which leads to subsequent axonal injury in older subjects (reduced NAA). Temporal progression and behavioral correlates of these MRSI changes deserve further exploration.

This study was supported by NIH NS-35359 and HD-24061. Dr Barker is the recipient of an established investigator award from the American Heart Association.

We thank Dr Jeff Duyn, National Institutes of Health, Bethesda, MD, for the MRSI pulse sequence.

References

1. National Institutes of Health Consensus Development Conference. Neurofibromatosis: conference statement. *Arch Neurol* 1988;45:575–578
2. Goldstein SM, Curless RG, Donovan Post MJ, Quencer RM.

- A new sign of neurofibromatosis on magnetic resonance imaging of children. *Arch Neurol* 1989;46:1222-1224
3. Duffner PK, Cohen ME, Seidel FG, Shucard DW. The significance of MRI abnormalities in children with neurofibromatosis. *Neurology* 1989;39:373-378
 4. Aoki S, Barkovich AJ, Nishimura K, et al. Neurofibromatosis types 1 and 2: cranial MR findings. *Radiology* 1989;172:527-534
 5. Seivick RJ, Barkovich AJ, Edwards MS, et al. Evolution of white matter lesions in neurofibromatosis type 1: MR findings. *AJR* 1992;159:171-175
 6. Itoh T, Magnaldi S, White RM, et al. Neurofibromatosis type 1: the evolution of deep gray and white matter MR abnormalities. *AJNR* 1994;15:1513-1519
 7. North K, Joy P, Yuille D, et al. Specific learning disability in children with neurofibromatosis type 1: significance of MRI abnormalities. *Neurology* 1994;44:878-883 (Comment)
 8. DiMario FJ Jr, Ramsby G. Magnetic resonance imaging lesion analysis in neurofibromatosis type 1. *Arch Neurol* 1998;55:500-505
 9. Denckla MB, Hofman K, Mazzocco MM, et al. Relationship between T2-weighted hyperintensities (unidentified bright objects) and lower IQs in children with neurofibromatosis-1. *Am J Med Genet* 1996;67:98-102
 10. DiPaolo DP, Zimmerman RA, Rorke LB, et al. Neurofibromatosis type 1: pathologic substrate of high-signal-intensity foci in the brain. *Radiology* 1995;195:721-724
 11. Castillo M, Green C, Kwock L, et al. Proton MR spectroscopy in patients with neurofibromatosis type 1: evaluation of hamartomas and clinical correlation [published erratum appears in *AJNR* 1995;16:808]. *AJNR* 1995;16:141-147
 12. Broniscer A, Gajjar A, Bhargava R, et al. Brain stem involvement in children with neurofibromatosis type 1: role of magnetic resonance imaging and spectroscopy in the distinction from diffuse pontine glioma. *Neurosurgery* 1997;40:331-337
 13. Gonen O, Wang ZJ, Viswanathan AK, et al. Three-dimensional multi-voxel proton MR spectroscopy of the brain in children with neurofibromatosis type 1. *AJNR* 1999;20:1333-1341
 14. Urenjak J, Williams SR, Gadian DG, Noble M. Proton nuclear magnetic resonance spectroscopy unambiguously identifies different neural cell types. *J Neurosci* 1993;13:981-989
 15. Duyn JH, Gillen J, Sobering G, et al. Multislice proton MR spectroscopic imaging of the brain. *Radiology* 1993;188:277-282
 16. Soher BJ, van Zijl PCM, Duyn JH, Barker PB. Quantitative proton spectroscopic imaging of the human brain. *Magn Reson Med* 1996;35:356-363
 17. Siegel S, Castellan NJ. Nonparametric statistics for the behavioral sciences. New York: McGraw-Hill, 1988
 18. Coutinho CMA, Jones AP, Gunawardena WJ. Assessment of brain hamartomas in children with neurofibromatosis using ¹H magnetic resonance spectroscopy. Presented at the ISMRM 7th Scientific Meeting and Exhibition, Philadelphia, 1999:1469
 19. Barker PB, Breiter SN, Soher BJ, et al. Quantitative proton spectroscopy of canine brain: in vivo and in vitro correlations. *Magn Reson Med* 1994;32:157-163
 20. Yamanouchi H, Kato T, Matsuda H, et al. MRI in neurofibromatosis type I: using fluid-attenuated inversion recovery pulse sequences. *Pediatr Neurol* 1995;12:286-290
 21. Carpenter MB. Human neuroanatomy. Baltimore: Williams and Wilkins, 1976
 22. Steen RG, Ogg R, Reddick WE, et al. Quantitative MR imaging of diffuse brain abnormality: T1 in patients with neurofibromatosis (NF-1) and other brain disorders. Presented at ISMRM 7th Scientific Meeting and Exhibition, Philadelphia, 1999:611
 23. Riccardi VM. Neurofibromatosis: phenotype, natural history, and pathogenesis. Baltimore: Johns Hopkins University Press, 1992
 24. Moore BD, Slopis JM, Schomer D, et al. Neuropsychological significance of areas of high signal intensity on brain MRI of children with neurofibromatosis. *Neurology* 1996;46:1660-1668

Scan Time Reduction in Proton Magnetic Resonance Spectroscopic Imaging of the Human Brain

Xavier Golay,^{1,2*} Joseph Gillen,^{1,2} Peter C.M. van Zijl,^{1,2} and Peter B. Barker^{1,2}

A simple technique is described for scan time reductions in proton magnetic resonance spectroscopic imaging (MRSI) of the human brain. Scan time is reduced by approximately 35% while preserving spatial resolution by reducing the field of view (FOV) and number of phase-encoding steps in the transverse direction of the brain. A multislice MRSI of the brain is demonstrated which takes approximately 20 min with a square FOV, and 13 min with a reduced FOV. The signal-to-noise ratio (SNR) in the reduced FOV scan was measured to be 15% lower than that of the full FOV scan, which is close to the expected theoretical value of 19% based on the square root of the scan time. The method can be applied with any sequence, and requires minimal software and no hardware modifications. Scan time in MRSI is minimized in this method by using FOVs no larger than the dimensions of the object to be imaged. The method may also be combined with other fast MRSI techniques to provide further scan time reductions. *Magn Reson Med* 47: 384–387, 2002. © 2002 Wiley-Liss, Inc.

Key words: spectroscopic imaging; scan time reduction; brain; magnetic resonance

Proton magnetic resonance spectroscopy (MRS) of the human brain is gaining acceptance as a diagnostic clinical technique (1,2). Currently, most examinations are performed using single voxel (SV) localization techniques (3), in part because of their commercial availability, but also because of their relatively short scan times (e.g., 5–10 min). However, one of the limitations of SV spectroscopy is its lack of brain coverage and information on metabolic heterogeneity. In contrast, multislice or 3D MRS imaging (MRSI) techniques provide good brain coverage and spatial resolution, but typically involve scan times on the order of 30 min, which limits their applicability to the general patient population. In particular, MRSI scan times may be too long for severely or acutely ill patients, such as those with acute stroke (4), or for young children without sedation or anesthesia (5).

The minimum scan time in conventional multidimensional proton MRSI is determined by the product of the repetition time (TR) and the required number of phase-encoding steps. Typically, scan times are longer than those

required to obtain sufficient signal-to-noise ratios (SNRs) if phase-encoding were not performed (i.e., SV experiments). For a multislice 2D MRSI experiment, the minimum TR is set by the number of slices acquired, and the time required for each slice, including the echo time (TE) and the length acquisition readout, water suppression, and lipid suppression elements. For example, when using a multislice 2D MRSI technique with outer-volume suppression (OVS), as originally proposed by Duyn et al. (6), a four-slice acquisition of a square 32×32 imaging matrix using a TR of 2.3 s will take approximately 39 min, and about 30 min with a circular *k*-space sampling scheme, reducing the number of encoding steps by 25% (7).

A number of approaches have been proposed and implemented for faster MRSI of the brain. These include the use of multiple spin-echoes (8), oscillating read gradients (9,10), and fast-imaging sequence readouts after a period of evolution under free precession (11,12). Each of these methods have been successfully demonstrated in the brain but have not become widely used for a variety of reasons, including lack of availability on commercial systems, more complicated data processing requirements, and reductions in SNR associated with the pulse sequence. In this work, we describe a simple modification to conventional 2D MRSI which allows a time-saving of approximately 25–35%. The method is based on exploiting the smaller dimensions of the brain in the left-right direction compared with the anterior-posterior direction, involves no changes to the pulse sequence, and does not involve any SNR losses other than those associated with the reduction in the scan time itself. By reducing both the FOV in the left-right dimension and the number of phase-encoding steps in proportion, spatial resolution is unaffected. Although this approach has been widely used in brain MRI for a number of years, there is no mention in the literature of any implementation of such a method for proton MRSI, although this method may be available commercially on some MR systems.

METHODS

Scans were recorded on a 21-year-old normal male subject. The protocol was approved by the Johns Hopkins Institutional Joint Committee on Clinical Investigation, and informed consent was obtained. All experiments were performed on a 1.5 Tesla Philips Gyroscan ACS NT (Philips Medical Systems, Best, The Netherlands) with a Powertrak 6000 gradient system (21 mT/m strength and 105 mT/m/ms slew rate) using the standard quadrature birdcage transmit/receive head coil. After collection of localizer images, a conventional multislice spin-echo 2D

*F.M. Kirby Research Center for Functional Brain Imaging, Kennedy Krieger Institute, Baltimore, Maryland.

²Russell H. Morgan Department of Radiology and Radiological Science, Johns Hopkins University School of Medicine, Baltimore, Maryland.

Grant sponsors: F.M. Kirby Center for Functional Brain Imaging of the Kennedy Krieger Institute; Philips Medical Systems; Grant sponsor: National Institutes of Health; Grant numbers: R21CA/RR91798; P41RR15241.

*Correspondence to: Xavier Golay, Ph.D., F.M. Kirby Research Center for Functional Brain Imaging, Kennedy Krieger Institute, 707 N. Broadway, Baltimore, MD 21205. E-mail: xgolay@mri.jhu.edu

Received 6 August 2001; revised 14 September 2001; accepted 17 September 2001.

© 2002 Wiley-Liss, Inc.
DOI 10.1002/mrm.10038

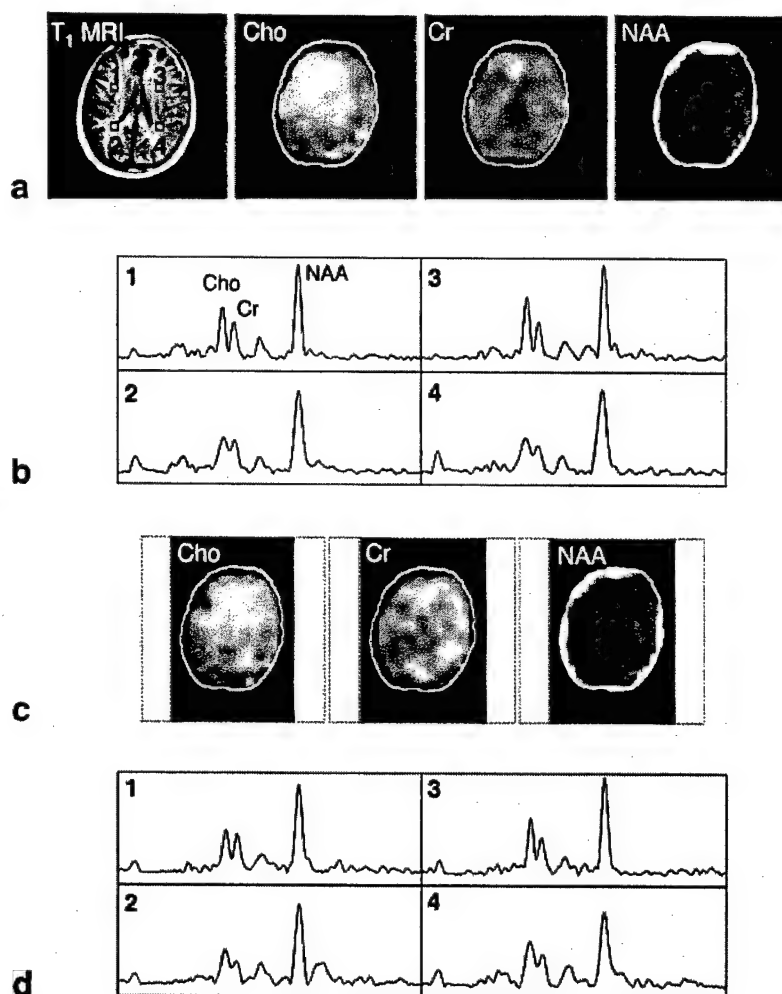


FIG. 1. **a:** T_1 -weighted and metabolic images (Cho, Cr, and NAA) from the middle slice of the three-slice MRSI performed with a square FOV. **b:** Selected spectra from the voxel locations in frontal and parietal lobes illustrated on T_1 -weighted localizer MRI. **c:** Metabolic images (Cho, Cr, and NAA) from the middle slice of the three-slice MRSI performed with a 68% reduced FOV in the left-right direction and a 7-min shorter scan time. **d:** Spectra are selected from the same regions as in Fig. 1b. Metabolic images and spectra are almost indistinguishable in terms of SNRs and resolution between the full and reduced FOV data sets.

MRSI scan (6) was recorded using the following parameters: FOV = 240×240 mm, slice thickness = 15 mm, gap = 2.5 mm, TR = 2000 ms, TE = 280 ms, 256 data points, spectral width = 1 kHz, with a circular phase-encoding scheme of 28×28 steps, giving a scan time of 20 min 30 s. Three axial slices were acquired with the lowest slice at the level of the thalamus, and the nominal voxel size was 1.1 cm^3 . The "real" voxel size after processing and spatial filtering is approximately double the nominal voxel size (7). A single chemical shift selective (CHESS) pulse was used for water suppression (13) followed by an octagonal OVS scheme for suppression of pericranial lipid signals in each slice (6). Then the same sequence was repeated, this time reducing the FOV to 16.3 cm in the left-right direction (68%), an acquisition matrix of 28×19 , while keeping all other parameters identical (i.e., same TR, TE, and nominal voxel size). The duration of this sequence was 13 min 22 s (i.e., approximately 7 min less than the full FOV sequence). After the second MRSI sequence, a dual gradient-echo scan was recorded for measurement of B_0 magnetic field homogeneity (14).

MRSI data was processed using the program "csx2k" (developed at Johns Hopkins University School of Medicine and available for download at <http://mri.kennedykrieger.org/>) (15). The original 256 data points in the time domain were zero-filled to 2048 prior to 3D fast Fourier transformation (FFT). For convenience, the routine "fftw" ("Fastest Fourier Transform in the West," <http://www.fftw.org/index.html>) was used, which allows fast multidimensional Fourier transforms to be performed on matrices whose dimensions are not a power-of-2 ($28 \times 28 \times 2048$, and $28 \times 19 \times 2048$). Prior to FFT, a cosine filter was applied in both spatial domains and an exponential filter corresponding to a 3-Hz line broadening was applied in the time domain. Time domain processing also included a susceptibility correction based on the field maps calculated from the double gradient-echo scans (14), and a high-pass filter (16) to remove the residual water signal. After Fourier transformation, magnitude spectra were calculated. Metabolic images were created by numerical integration over the following frequency ranges: choline (Cho) 3.34–3.14 ppm; creatine (Cr) 3.14–2.94 ppm; and N-acetyl aspartate (NAA) 2.22–1.82 ppm. They were

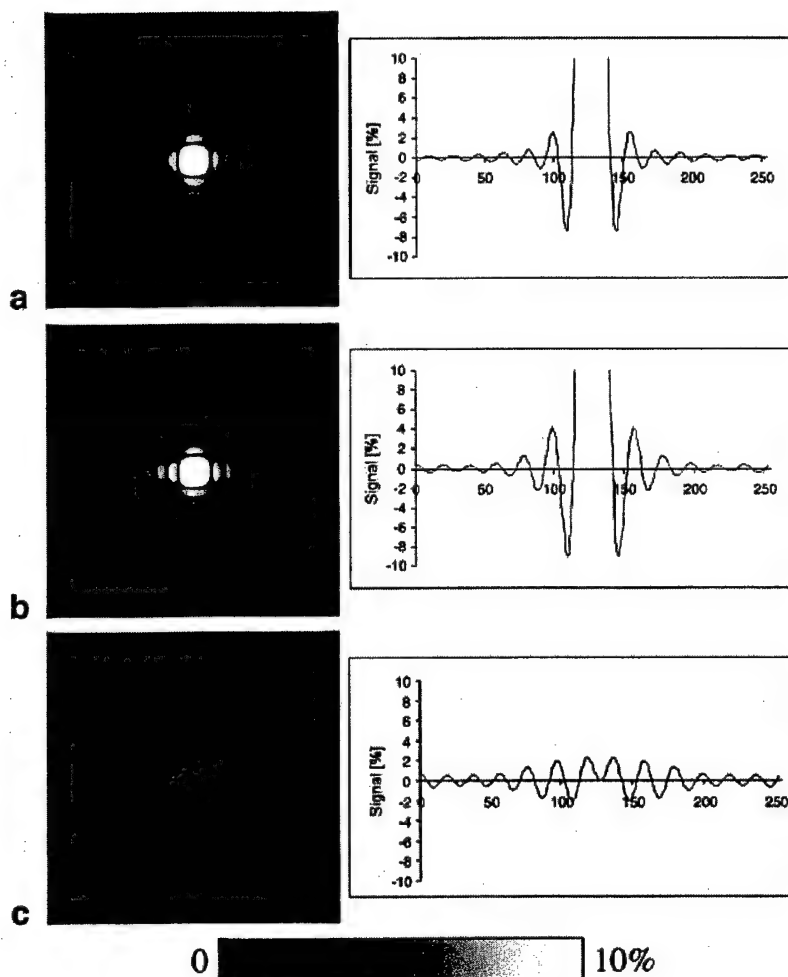


FIG. 2. Simulations of the 2D PSFs for (a) 28×28 matrix, (b) 28×19 matrix, and (c) the difference of **b** - **a**. The gray-scale range is set to display zero to 10% of the maximum signal intensity in order to visualize the sidelobes. Together with each gray-scale image, a profile at $y = 0$ is shown. It can be seen that the central lobe is almost identical in **a** and **b**, but that there are slightly less circular symmetry and increased sidelobe intensity in the reduced FOV (horizontal) direction in **b**.

linearly interpolated by a factor of 8 (either to 224×224 or to 224×152) for display.

Measurement of the SNR in multiple voxels in both data sets was performed by comparing the height of the NAA peak (at 2.02 ppm) with the root-mean-square noise level between 8 and 12 ppm, where no signals are expected at long TE. A total of 80 spectra were measured from the central slice in each dataset from an 8×10 voxel rectangular region of interest chosen to exclude any signals from the skull or edges of the brain.

Simulations of the MRSI point spread functions (PSFs) for both square and rectangular FOVs were calculated by 2D FFT of the MRSI sampling functions (28 ± 28 , and 28 ± 19) including circular k -space sampling, cosine filtration, and zero-filling to 256 ± 256 points.

RESULTS

MRSI images and spectra were successfully acquired with a rectangular FOV of 68% in the left-right direction, and were visually indistinguishable from those recorded with a square FOV (Fig. 1). In MRSI, as in two-dimensional high resolution nuclear magnetic resonance spectroscopy (17,18), phase en-

coding has the same effect on the SNR as averaging, provided the voxel size does not change. In the example provided here, the reduced FOV scan duration was approximately 65% of the full FOV scan, and the theoretical SNR should therefore be approximately 81%. The reduction in scan time to 65% (and not 68%) is due to the rounding algorithm used by the scanner in the determination of the number of measured data points when combining a circular sampling with the reduced FOV. For the 80 voxels measured in each data set, on average the SNR was 29.2 for the full FOV, and 24.9 for the reduced FOV, i.e., the experimentally determined SNR was 85% of that of the full FOV scan—very close to the predicted theoretical value of 81%.

Figure 2 shows the calculated 2D PSFs for the square and rectangular FOV MRSI experiments, together with the corresponding profiles at $y = 0$. It can be seen that the area of the central lobe is virtually identical in both cases, but that the outer lobes of the PSF are slightly different, and in particular the circular symmetry of the 28×28 phase-encoding pattern is slightly disrupted with the rectangular FOV. This is because the rectangular FOV sampling pattern is not completely circularly symmetric in k -space (7). However, the

difference in PSFs (Fig. 2c) between the two approaches is extremely small, and only manifests as a minimally increased side-lobe intensity in the direction of the reduced FOV. The actual voxel size—given by the integral of the PSF—was 2.52 and 2.58 times the nominal voxel size in the full and reduced FOV scans, respectively (i.e., virtually identical (2.3% voxel size increase)).

DISCUSSION

In MRSI (and MRI), for a fixed desired spatial resolution, there is a linear relationship between the FOV and the number of phase-encoding steps. Therefore, when the scan time is limited by encoding time, rather than by time-averaging required to attain sufficient SNR, the shortest scan times are attainable when the FOV is set to the minimum consistent with the requirement to avoid aliasing. Since the dimensions of the brain are different in each direction, this is best achieved with a rectangular FOV. Provided that the number of phase-encoding steps is reduced in proportion to the FOV while maintaining the maximum gradient amplitude, the nominal spatial resolution is unchanged (i.e., fewer phase-encoding steps are applied in the left-right direction, but with a greater increment in *k*-space from one step to the next). SNR is decreased in proportion to the square root of the number of scans, so it is only decreased appreciably if very large FOV reductions (e.g., << 50%) are applied.

The method proposed in this work allows for a modest reduction of scanning time, and cannot therefore be compared with other, faster MRSI techniques that may offer greater scan time reductions (8–11,18). However, it is simple to apply and can be used with conventional MRSI techniques with minimal modifications. Although rectangular FOVs have been used in the past for 2D or 3D MRSI using point-resolved spectroscopy (PRESS) prelocalization (19,20), these were restricted to relatively small volumes of the head and did not have full brain coverage. It should also be recognized that FOV reduction can be applied in conjunction with other fast MRSI techniques to provide further scan time reductions.

When the FOV is reduced to less than the dimensions of the head, aliasing will occur (and the data will be uninterpretable) unless PRESS localization and/or saturation bands are used to eliminate signal outside of the FOV. However, if multichannel phased-array head coils are available, the sensitivity encoding (SENSE) algorithm (21) can be used to unfold and sensitivity-correct the multichannel MRSI data (22). SENSE-MRSI appears to be a particularly favorable method for fast MRSI, since the SNR losses associated with reduced scan time are partially offset by the use of local RF coils with higher sensitivity than volume head coils. On the other hand, SENSE can only be applied if phased-array head coils and multichannel receivers are available, and, at present, there is limited commercial availability of these features. In contrast, the reduced FOV technique proposed here can be used with conventional single-channel RF head coils, albeit with a smaller reduction in scan time compared to SENSE.

In summary, reduced (rectangular) FOV MRSI can give significant scan time savings (e.g., approximately 7 min in the current example) with only negligible changes in spatial

resolution and small reductions in SNRs, and without pulse sequence or hardware modifications, making MRSI a good clinical alternative to SV MRS, for which 5–10 min of signal averaging is necessary. In proton MRSI of the brain, minimum scan times can be attained by setting the FOV no larger than the dimensions of the region of the brain to be imaged.

ACKNOWLEDGMENTS

This work was done during the tenure of an Established Investigatorship from the American Heart Association (to P.B.B.).

REFERENCES

- Constantinidis I. Magnetic resonance spectroscopy and the practicing neurologist. *Neurologist* 1998;4:77–98.
- Ross B, Michaelis T. Clinical applications of magnetic resonance spectroscopy. *Magn Reson Q* 1994;10:191–247.
- Frahm J, Bruhn H, Gyngell ML, Merboldt KD, Hanicke W, Sauter R. Localized high-resolution proton NMR spectroscopy using stimulated echoes: initial applications to human brain *in vivo*. *Magn Reson Med* 1989;9:79–93.
- Barker PB, Gillard JH, van Zijl PCM, Soher BJ, Hanley DF, Agildere AM, Oppenheimer SM, Bryan RN. Acute stroke: evaluation with serial proton MR spectroscopic imaging. *Radiology* 1994;192:723–732.
- Horská A, Naidu S, Herskovits EH, Wang PY, Kaufmann WE, Barker PB. Quantitative proton MR spectroscopic imaging in early Rett syndrome. *Neurology* 2000;54:715–722.
- Duyn JH, Gillen J, Sohering G, van Zijl PCM, Moonen CTW. Multislice proton MR spectroscopic imaging of the brain. *Radiology* 1993;188:277–282.
- Maudsley AA, Matson GB, Hugg JW, Weiner MW. Reduced phase encoding in spectroscopic imaging. *Magn Reson Med* 1994;31:645–651.
- Duyn JH, Moonen CT. Fast proton spectroscopic imaging of human brain using multiple spin-echoes. *Magn Reson Med* 1993;30:409–414.
- Adelsteinsson E, Irarrazabal P, Topp S, Meyer C, Macovski A, Spielman DM. Volumetric spectroscopic imaging with spiral-based *k*-space trajectories. *Magn Reson Med* 1998;39:889–898.
- Posse S, Tedeschi G, Risinger R, Ogg R, Le Bihan D. High speed ¹H spectroscopic imaging in human brain by echo planar spatial-spectral encoding. *Magn Reson Med* 1995;33:34–40.
- Norris DG, Dreher W. Fast proton spectroscopic imaging using the sliced *k*-space method. *Magn Reson Med* 1993;30:641–645.
- Dreher W, Leibfritz D. Improved proton spectroscopic U-FLARE imaging for the detection of coupled resonances in the rat brain *in vivo*. *Magn Reson Imaging* 1999;17:611–621.
- Haase A, Frahm J, Hanicke W, Matthai D. ¹H NMR chemical shift selective imaging. *Phys Med Biol* 1985;30:341–344.
- Barker PB, Szopinski K, Horská A. Metabolic heterogeneity at the level of the anterior and posterior commissures. *Magn Reson Med* 2000;43:348–354.
- Soher BJ, van Zijl PCM, Duyn JH, Barker PB. Quantitative proton spectroscopic imaging of the human brain. *Magn Reson Med* 1996;35:356–363.
- Marion D, Ikura M, Bax A. Improved solvent suppression in one- and two-dimensional NMR spectra by convolution of time-domain data. *J Magn Reson* 1989;84:425–430.
- Ernst RR, Bodenhausen G, Wokaun A. Principles of nuclear magnetic resonance in one and two dimensions. Oxford, UK: Oxford University Press; 1987. p 352.
- Pohmann R, von Kienlin M, Haase A. Theoretical evaluation and comparison of fast chemical shift imaging methods. *J Magn Reson* 1997;129:145–160.
- Nelson SJ, Vigneron DB, Star-Lack J, Kurhanewicz J. High spatial resolution and speed in MRSI. *NMR Biomed* 1997;10:411–422.
- Star-Lack J, Vigneron DB, Pauly J, Kurhanewicz J, Nelson SJ. Improved solvent suppression and increased spatial excitation bandwidths for three-dimensional PRESS CSI using phase-compensating spectral/spatial spin-echo pulses. *J Magn Reson Imaging* 1997;7:745–757.
- Pruessmann KP, Weiger M, Scheidegger MB, Boesiger P. SENSE: sensitivity encoding for fast MRI. *Magn Reson Med* 1999;42:952–962.
- Dydyk U, Weiger M, Pruessmann KP, Meier D, Boesiger P. Sensitivity-encoded spectroscopic imaging. *Magn Reson Med* 2001;46:713–722.

AQ: 1

Rapid Method for Correction of CSF Partial Volume in Quantitative Proton MR Spectroscopic Imaging

A. Horská,¹ V.D. Calhoun,² D.H. Bradshaw,³ and P.B. Barker^{1,4*}

Partial volume effects with cerebrospinal fluid (CSF), if uncorrected, can lead to underestimation of metabolite concentrations in quantitative proton magnetic resonance spectroscopic imaging (MRSI) of the brain. A rapid method for the correction of CSF partial volume effects is described based on selective CSF imaging using long echo time (TE) fast spin echo (FSE) magnetic resonance imaging (MRI). In order to achieve maximum suppression of signal from brain parenchyma, the FSE sequence is coupled with an inversion recovery (IR) pulse. Scan time is minimized using single shot (SS) IR-FSE. The method is validated against a current "gold standard" for the determination of CSF volumes, namely, segmented 3D spoiled gradient-echo (SPGR) scans. Excellent agreement in CSF percentage determined by the two methods was found (linear regression analysis: slope = 0.99 ± 0.02 , intercept = 2.08 ± 0.45 ; mean \pm standard errors, $R = 0.93$) in pooled data from four healthy subjects. An example of the use of SS-IR-FSE for partial volume correction in a leukodystrophy patient with T_2 hyperintense lesions is demonstrated. The SS-IR-FSE method is a simple and rapid method for applying partial volume corrections in quantitative proton MRSI, which may be of particular value in the clinical environment when time constraints do not allow longer, perhaps more accurate segmentation methods to be used. *Magn Reson Med* 48:000–000, 2002. © 2002 Wiley-Liss, Inc.

AQ: 2

Key words:

Quantitative determination of brain metabolite concentrations in proton MR spectroscopic imaging (MRSI) depends on a knowledge of the amount of cerebrospinal fluid (CSF) in each voxel, especially for cortical gray matter and periventricular regions wherein appreciable CSF contamination may occur. Numerous MRI-based approaches have been suggested for the segmentation of intracranial spaces into different tissue types and CSF (1), including methods based on T_1 or T_2 contrast (2–4) previously used for CSF correction schemes for proton MRSI. However, all of these methods may add significantly to the length of the combined MRI and MRSI examination, and postprocessing may also be time-consuming.

In this work, a new approach based on direct imaging of CSF based on long-TE fast spin-echo (FSE) MRI (5) is described. This approach has previously been applied to

single-voxel spectroscopy (6), but has not previously been used in MRSI. Improved brain parenchyma suppression and reduced scan time is achieved by using single shot inversion recovery (SS IR) FSE, and the postprocessing is also relatively simple.

METHODS

Subjects

Four healthy subjects (three males and one female, 43 \pm 2.5 years old) were examined. The MRI/MRSI protocol was approved by the Johns Hopkins University Joint Committee on Clinical Investigations, and informed consent was obtained prior to the examination. A 23-year-old woman diagnosed with idiopathic leukodystrophy was also scanned. The patient was referred for clinical proton MRSI examination to evaluate the extent and etiology of white matter disease.

MR Protocol

Experiments were performed on a 1.5T GE Signa LX MR scanner (General Electric Medical Systems, Milwaukee, WI) using the standard quadrature birdcage head coil.

Proton MRSI was performed using a multislice SE sequence with outer volume suppression (7). Three oblique slices were measured with a 15-mm thickness and a gap of 2.5 mm (TR = 1700 ms, TE = 280 ms, acquisition matrix = $32 \times 32 \times 256$, FOV = 24 cm). T_1 -weighted SE MR images (15-mm slice thickness, TR = 400 ms, TE = 20 ms) were recorded at the same slice locations as the MRSI data set for anatomical correlation. Metabolite concentrations (mM) (per unit voxel size) were measured using the phantom replacement methodology (8), after which the parenchymal concentration was calculated using the correction factor $[M]_{\text{corr}} = [M] * [100/(100 - \% \text{CSF})]$ (mM), where the %CSF was determined as described below.

For selective CSF imaging, an SS IR T_2 -weighted FSE sequence (TI = 425 ms, TE = 346 ms, one echo, echo train length = 128, echo spacing = 5.08 ms, pulse bandwidth = 4 kHz, receiver bandwidth = 62.5 kHz, three slices, slice thickness = 15 mm, slice gap = 2.5 mm, FOV = 24×24 cm, matrix size = 256×128 , one acquisition, number of dummy scans = 0, scan time = 3 s) was recorded at the same slice locations as the MRSI data.

For validation of the SS-IR-FSE method, the results were compared to those obtained from a conventional 3D spoiled gradient echo (SPGR) scan. The axial 3D SPGR was performed with the following parameters: TR = 35 ms, TE = 5 ms, flip angle = 45° , slice thickness = 1.5 mm, 124 slices, FOV = 24×18 cm, matrix size = $256 \times 128 \times 124$, one acquisition, scan time = 7 min 14 s.

¹Division of Neuroradiology, Russell H. Morgan Department of Radiology and Radiological Science, Johns Hopkins University, Baltimore, Maryland.

²Department of Psychiatry, Johns Hopkins University, Baltimore, Maryland.

³Thomas C. Jenkins Department of Biophysics, Johns Hopkins University, Baltimore, Maryland.

⁴F.M. Kirby Research Center for Functional Brain Imaging Kennedy Krieger Institute, Baltimore, Maryland.

Grant sponsor: NIH; Grant numbers: RO3AG17364; P41 RR15241.

*Correspondence to: P.B. Barker, Department of Radiology, MRI 143C, Johns Hopkins University School of Medicine, 600 N. Wolfe St., Baltimore, MD 21287. E-mail: barker@mri.jhu.edu

Received 30 January 2002; revised 26 April 2002; accepted 1 May 2002.

DOI 10.1002/mrm.10242

Published online in Wiley InterScience (www.interscience.wiley.com).

© 2002 Wiley-Liss, Inc.

Since it may be difficult to identify pixels with 100% CSF in subjects with small ventricles, all experiments were performed with an external reference (distilled water) positioned close to the head of the subject. To verify the concordance of the CSF and water signal intensities, T_2 relaxation times of both water and CSF were determined using SS echo planar imaging (EPI) with flow compensation, using the following parameters: TE = 138, 338, 538, 738, and 938 ms; slice thickness = 5 mm; slice gap = 2 mm.

Image Analysis

A Java-based computer program was used for segmentation of the SPGR images ("blox," <http://pni.med.jhu.edu/blox>). Intensity variations in the SPGR images due to variable flip angle across the slice-selective slab were corrected by fitting a third-order polynomial function to the image intensity. (Note, however, that since the commercial quadrature birdcage head coil is extremely homogeneous over the volume of the brain covered in these experiments, no corrections for RF inhomogeneity were performed in either the SS-IR-FSE or the SPGR images). Ten 1.5-mm-thick, inhomogeneity-corrected slices were extracted to match the 15-mm slice thickness of the MRSI and SS-IR-FSE scans. High-resolution percentage maps of each tissue type (gray matter, white matter, and CSF) were created by summation of these 10 slices.

For pixel-by-pixel comparison of the SS-IR-FSE and the segmented CSF images, the images were scaled relative to the maximum intensity in each data set (in the lateral ventricles, corresponding to 100% CSF) and to the intensity of the external water reference (in the SS-IR-FSE images only). In the SS-IR-FSE images, the minimum pixel intensity from brain parenchyma region identified to contain no CSF (i.e., deep white matter) was subtracted from all data points. Finally, to calculate the amount of CSF in each MRSI voxel, the scaled, segmented SPGR and SS-IR-FSE images were convolved with the MRSI point spread function for each region of interest (ROI). The 2D point spread function was computed as follows: a 32×32 matrix was constructed based on the cosine and Fermi filters used for the MRSI processing, zero-filled to 256×256 data points after applying the spatial filters, followed by Fourier transformation.

To perform a pixel-by-pixel comparison of segmented selective CSF SS-IR-FSE and CSF SPGR image intensities, Model II (reduced major axis) (9) linear regression parameters were derived from standard least-squares analysis (Statview; Abacus Concepts, Berkeley, CA). The paired t -test was used to examine differences between T_2 values of CSF and the water reference, and their respective signal intensities in the SS-IR-FSE images. Statistical significance was set to $P < 0.05$. The data are presented as means \pm standard deviations, unless otherwise specified.

RESULTS

In an SE sequence, the transverse magnetization of gray and white matter is $\leq 3\%$ at a TE of 346 ms (the longest TE available on the scanner used for these experiments), while the CSF magnetization is 87%. For the computation,

T_2 values of 101 ms for gray matter, and 92 ms for white matter (10) were used. The T_2 value of the CSF was determined from the SS-EPI experiments to be 2406 ± 99 ms ($N = 4$ subjects), although it should be recognized that different decay rates may be found for the SS-FSE experiments because of the effects of diffusion, eddy currents, and imperfect refocusing. Additional suppression of brain tissue signal was obtained using an inversion preparation pulse (11) by exploiting the large differences in T_1 between gray matter, white matter, and CSF (10). For normal brain, a choice of TI = 425 ms provided further suppression of both gray and white matter, while still leaving 70% of the inverted CSF signal.

Comparison of SS-IR-FSE selective brain CSF images acquired at the level of lateral ventricles in four control subjects with images obtained by segmentation of the SPGR scan showed an excellent agreement between the two methods. The results of the regression analysis of the CSF percentage in individual voxels, including the ventri-

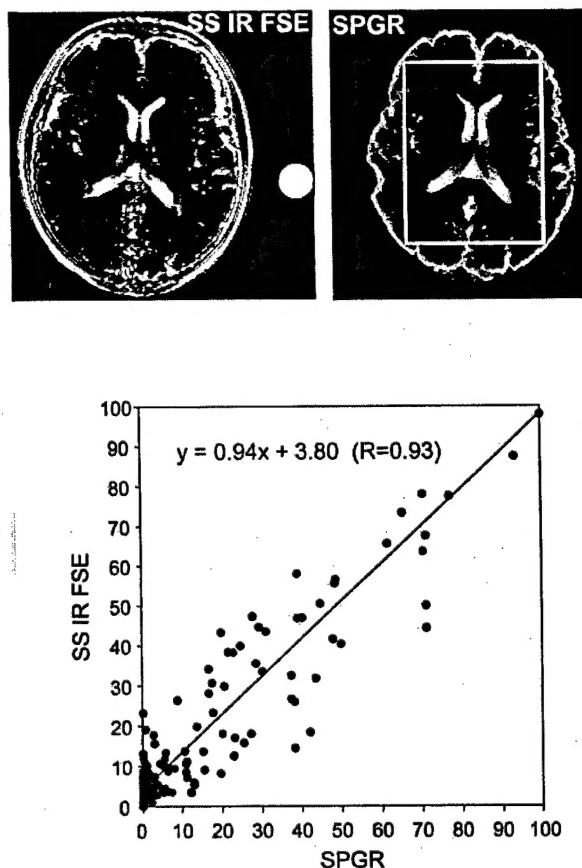


FIG. 1. SS-IR-FSE image of the CSF recorded at the level of lateral ventricles and segmented CSF image from the SPGR scan in a 45-year-old healthy female subject. Results of linear regression analysis of scaled image intensities between the segmented SPGR and the FSE images are shown. Regression analysis was performed in a selected ROI (shown in the SPGR image) to avoid regions with bright rim artifact in the SPGR image (the SPGR analysis procedure did not differentiate between the extracortical CSF and the skull).

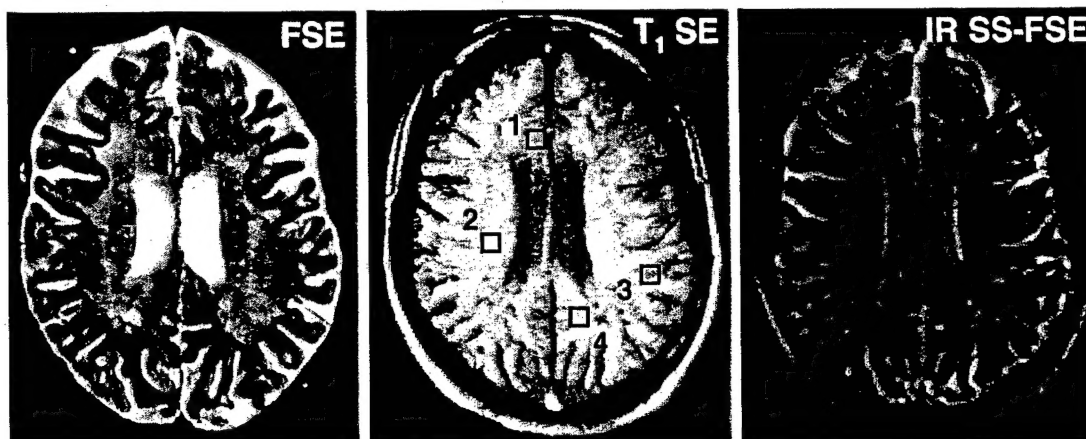


FIG. 2. Standard FSE T_2 -weighted, T_1 SE localizer, and SS-IR-FSE images of a 23-year-old woman with idiopathic leukodystrophy. ROI voxel locations for metabolite quantitation are indicated on the T_1 localizer image. The percentage of CSF contained in the depicted voxels is shown in Table 1. Despite extensive T_2 hyperintensity on FSE T_2 MRI, the SS-IR-FSE image shows no T_2 "shine-through" in these regions.

cles, white matter, and midline gray matter, between the two sets of images were: slope = 0.99 ± 0.02 , intercept = 2.08 ± 0.45 (\pm standard errors), $R = 0.93$, pooled data in all four subjects. (Within the four individuals, slopes were 0.92, 0.94, 0.96, and 1.05, and the intercepts were -0.45, 3.80, 3.20, and 2.11, respectively (with 100% CSF corresponding to a value of 100). Figure 1 shows an SS-IR-FSE and a corresponding SPGR segmented image obtained at a level of lateral ventricles in one subject, and the results of the regression analysis. The bright rim artifact in the CSF image calculated from the SPGR scan is due to the SPGR analysis procedure, which did not differentiate between the extracortical CSF and the skull (both appear dark on the SPGR images). Therefore, these regions were avoided for comparison of CSF images.

No significant differences were found between the T_2 values of the water reference (2365 ± 244 ms, $N = 4$) and the CSF (2406 ± 99 ms, $N = 4$) ($P = 0.67$, paired t -test) and between the signal intensities of pixels identified as containing 100% CSF and the external water reference signal intensity ($P = 0.75$, paired t -test). Therefore, an external standard of pure water can be used to calibrate the signal intensity of 100% CSF in normal volunteers.

In patients with brain pathologies, which manifest as T_2 hyperintensities on MRI (i.e., with long T_2 values), the SS-IR-FSE provides sufficient suppression of the brain parenchyma. The SS-IR-FSE sequence was applied for selective CSF imaging in a patient with idiopathic leukodystrophy (Fig. 2). While the T_2 FSE image shows a pronounced diffuse white matter hyperintensity, these areas appear dark on the SS-IR-FSE images, indicating the use of the SS-IR-FSE sequence as an adequate approach for CSF correction in patients with T_2 hyperintense lesions. Table 1 gives corrected concentrations of choline (Cho), creatine (Cr), and N-acetyl aspartate (NAA) in selected cortical, periventricular, and deep white matter regions. Of these regions, the largest CSF correction (27%) was required in the frontal medial region, while only a 3% CSF correction was needed in the affected white matter, which showed moderately reduced concentrations of all metabolites compared to other regions.

DISCUSSION

To account for CSF presence in MRSI, previous studies have used various techniques of image segmentation, based on T_1 (4,12-14) or T_1 and T_2 characteristics of the cerebral tissue classes (2,3,15,16). Although these methods of volumetric quantitation can be used both to assess the CSF partial volume effects and to examine differences in metabolite composition between gray and white matter, their accuracy may vary (17). Also, their scan time is relatively long (e.g., ranging from 5 min 47 s (15) to 12 min (12)) compared to the method proposed here (3 s for the SS-IR-FSE) and they may require considerable processing time. In contrast, the processing of the SS-IR-FSE images is fast and simple, since no registration or segmentation is required.

There are several potential sources of error, which should be recognized in determining CSF levels using SS-IR-FSE. To calibrate the signal intensity to percentage of CSF, it is necessary to identify pixels in the image, which contain 0% and 100% CSF, respectively. The deep white matter was used for determination of signal intensity corresponding to 0% CSF (the lower limit of the regression line). However, in some instances, such as in a largely atrophic brain, finding the lower limit of the regression line may be problematic. Our experiments performed in healthy individuals showed that the lower limit was on average $6.4\% \pm 0.5\%$ of the maximum signal intensity. Therefore, in a severely atrophic brain, where no region corresponding to 0% CSF can be reliably identified, the signal intensity corresponding to 0% CSF can be measured from the noise background of the image without introduc-

Table 1
Corrected Metabolite Concentrations (mM) in Regions Depicted in Figure 2

Region	% CSF	[Cho] _{corr}	[Cr] _{corr}	[NAA] _{corr}
Medial frontal	27.0	2.1	10.8	8.2
White matter lesion	3.1	1.9	4.1	5.3
Parietal	25.3	1.8	8.4	7.0
Parietal periventricular	19.5	1.7	7.6	6.9

ing significant error (e.g., less than 5%). Determination of upper and lower regression limits may be improved by recording SS-IR-FSE images with smaller slice thicknesses, which have less partial volume effects. This would involve the acquisition of a larger number of slices to match the MRSI brain coverage; however, only a small increase in scan time would occur since the method is single-shot. Processing would also be slightly more complicated, since several slices would have to then be summed to match the MRSI slice thickness.

The signal from a pixel in the lateral ventricles was used as a reference for pure (100%) CSF (as used previously in Ref. 6). Since the SS-IR-FSE images are performed at the same slice thickness as MRSI (15 mm in this case), it may not be trivial to identify such pixels, particularly in subjects with small CSF spaces. As an alternative, an external water reference can be used, which was found here to have the same proton density and T_2 as CSF in normal volunteers. However, it should be noted that this approach is sensitive to both B_1 inhomogeneity and potential changes in CSF T_2 (which might occur for several regions, such as changes in protein content, oxygenation, and subarachnoid hemorrhage (10)).

Another potential source of error is the effect of CSF flow on FSE signal intensity (18). Flow is known to reduce signal intensity in FSE images; however, this is only a problem if CSF flow velocities are large enough, and are also different between different regions of the image (i.e., different CSF spaces). The good correlation observed between the SS-IR-FSE method and CSF levels determined from the flow-insensitive SPGR approach suggests that CSF flow effects are not a significant problem under the conditions used here.

The final source of error to be considered is the failure to suppress signal from brain edema or solid lesions when changes in T_1 and T_2 relaxation occur. Simulations over a range of T_1 and T_2 values typically encountered under pathological values indicate that the SS-IR-FSE method (with the timing parameters used here) gives suppression values greater than 98%. Although the T_2 values of edema and many lesions are larger than normal tissue (1.1–1.5 times larger than T_2 of normal white matter), these values are still much shorter than those of CSF (19). Therefore, the SS-IR-FSE technique should be adequate to suppress signal from both edematous tissue and brain lesions. However, it should also be recognized that the method described here does not provide a correction scheme for the apparent dilution of metabolite concentrations by vasogenic edema if intracellular (or $\text{mmol} \cdot \text{kg}^{-1}$ w.w. brain tissue) concentration estimates are required.

Other fast imaging approaches could also be used for selective CSF imaging, such as magnetization prepared rapid gradient echo imaging (MP-RAGE) or EPI. SS-IR-FSE was selected in the current example because it is becoming commonly available on clinical MRI scanners, is well suited to long-TE imaging, and is less prone to spatial distortions or signal intensity artifacts due to susceptibility effects than EPI.

In conclusion, the method presented here provides a very fast and simple means of determining regional CSF content based on long-TE FSE imaging. The method proposed is a practical approach that can be conveniently

used in a clinical setting, where the extremely short scan times and simple analysis may be advantageous over other, perhaps more accurate methods that are more time-consuming. The method is particularly suited for partial volume correction in proton MRSI experiments, but can also be used for single-voxel spectroscopy. For studies in which sufficient scan time is available, other methods for CSF segmentation (2–4) may perhaps provide more accurate determination of regional CSF content.

ACKNOWLEDGMENTS

We thank Dr. Jeff Duyn and Dr. Jan Willem van der Veen (NIH) for the ^1H MRSI pulse sequence.

REFERENCES

1. Pham DL, Xu C, Prince JL. Current methods in medical image segmentation. *Annu Rev Biomed Eng* 2000;2:315–337.
2. Lim KO, Spielman DM. Estimating NAA in cortical gray matter with applications for measuring changes due to aging. *Magn Reson Med* 1997;37:372–377.
3. Lundbom N, Barnett A, Bonavita S, Patronas N, Rajapakse J, Tedeschi, Di Chiro G. MR image segmentation and tissue metabolite contrast in ^1H spectroscopic imaging of normal and aging brain. *Magn Reson Med* 1999;41:841–845.
4. Hetherington HP, Pan JW, Mason GF, Adams D, Vaughn MJ, Twieg DB, Pohost GM. Quantitative ^1H spectroscopic imaging of human brain at 4.1 T using image segmentation. *Magn Reson Med* 1996;36:21–29.
5. Hennig J, Friedburg H, Ott D. Fast three-dimensional imaging of cerebrospinal fluid. *Magn Reson Med* 1987;5:380–383.
6. Brooks JC, Roberts N, Kemp GJ, Martin PA, Whitehouse GH. Magnetic resonance imaging-based compartmentation and its application to measuring metabolite concentrations in the frontal lobe. *Magn Reson Med* 1999;41:883–888.
7. Duyn JH, Gillen J, Sobering G, van Zijl PCM, Moonen CT. Multisection proton MR spectroscopic imaging of the brain. *Radiology* 1993;188:277–282.
8. Soher BJ, van Zijl PCM, Duyn JH, Barker PB. Quantitative proton MR spectroscopic imaging of the human brain. *Magn Reson Med* 1996;35:356–363.
9. Sokal RR, Rohlf FJ. *Biometry*. 2nd ed. New York: W.H. Freeman; 1981. p 547–555.
10. Bottomley PA, Hardy CJ, Argersinger RE, Allen-Moore G. A review of ^1H nuclear magnetic resonance relaxation in pathology: are T_1 and T_2 diagnostic? *Med Phys* 1987;14:1–37.
11. Rusinek H, de Leon MJ, George AE, Stylopoulos LA, Chandra R, Smith G, Rand T, Mourino M, Kowalski H. Alzheimer disease: measuring loss of cerebral gray matter with MR imaging. *Radiology* 1991;178:109–114.
12. Pan JW, Twieg DB, Hetherington HP. Quantitative spectroscopic imaging of the human brain. *Magn Reson Med* 1998;40:363–369.
13. Noworolski SM, Nelson SJ, Henry RG, Day MR, Wald LL, Star-Lack J, Vigneron DB. High spatial resolution ^1H -MRSI and segmented MRI of cortical gray matter and subcortical white matter in three regions of the human brain. *Magn Reson Med* 1999;41:21–29.
14. McLean MA, Woermann FG, Barker GJ, Duncan JS. Quantitative analysis of short echo time (^1H -MRSI) of cerebral gray and white matter. *Magn Reson Med* 2000;44:401–411.
15. Doyle TJ, Bedell BJ, Narayana PA. Relative concentrations of proton MR visible neurochemicals in gray and white matter in human brain. *Magn Reson Med* 1995;33:755–759.
16. Schuff N, Amend DL, Meyerhoff DJ, Tanabe JL, Norman D, Fein G, Weiner MW. Alzheimer disease: quantitative ^1H -1 MR spectroscopic imaging of frontoparietal brain. *Radiology* 1998;207:91–102.
17. Bedell BJ, Narayana PA. Volumetric analysis of white matter, gray matter, and CSF using fractional volume analysis. *Magn Reson Med* 1998;39:961–969.
18. Alexander AL, Buswell HR, Sun Y, Chapman BE, Tsuruda JS, Parker DL. Intracranial black-blood MR angiography with high-resolution 3D fast spin echo. *Magn Reson Med* 1998;40:298–310.
19. Darwin RH, Drayer BP, Riederer SJ, Wang HZ, MacFall JR. T_2 estimates in healthy and diseased brain tissue: a comparison using various MR pulse sequences. *Radiology* 1986;160:375–381.